USE OF REMOTE SENSING AND MACHINE LEARNING TECHNIQUES FOR RESILIENT INFRASTRUCTURE HEALTH MONITORING

by

SEYEDEHNARGES TAHAEI YAGHOUBI

(Under the Direction of S. Sonny KIM)

ABSTRACT

This dissertation investigates the use of weigh-in-motion (WIM) and continuous count station (CCS) data, remote sensing, and machine learning techniques to maintain resilient infrastructures and employs a deep learning methodology to detect the surface distresses of pavements. WIM and CCS technology obtain many useful traffic information as vehicles move along the roads. Remote sensing methods offer tools to replace or complement existing traditional methods of pavement management systems and can serve many needs of transportation agencies. Machine learning techniques, also facilitate pavement management routine by creating models and predicting the roads performance and their deterioration status.

This study investigates the predictions of resilient infrastructure distress situation by analyzing the historical spectra of flexible pavement road sections derived from Sentinel-2 and PlanetScope satellite images. The study also attempts to utilize a deep learning-based algorithm for predicting the pavement distresses using the images taken from interstate roads of Georgia.

The recognition accuracy of the prediction model determines whether the remote sensing platform accompanied by machine learning approaches and Deep Neural Network (DNN) algorithms can be utilized as smart monitoring platforms for distress evaluation of the asphalt infrastructures and further maintenance activities.

INDEX WORDS: Satellite Images; Remote Sensing; Machine Learning; Weigh-In-Motion (WIM) Data; Pavement Distress; Pavement Mechanistic-Empirical (ME) Design; Deep Learning; Crack Identification.

USE OF REMOTE SENSING AND MACHINE LEARNING TECHNIQUES FOR RESILIENT INFRASTRUCTURE HEALTH MONITORING

by

SEYEDEHNARGES TAHAEI YAGHOUBI

B.Sc., University of Tabriz, Iran, 2012

M.Sc., Azarbaijan Shahid Madani University, Tabriz, Iran, 2015

A Dissertation Submitted to the Graduate Faculty of The University of Georgia in Partial Fulfillment of the Requirements for the Degree

DOCTOR OF PHILOSOPHY

ATHENS, GEORGIA

2022

© 2022

SEYEDEHNARGES TAHAEI YAGHOUBI

All Rights Reserved

USE OF REMOTE SENSING AND MACHINE LEARNING TECHNIQUES FOR RESILIENT INFRASTRUCTURE HEALTH MONITORING

by

SEYEDEHNARGES TAHAEI YAGHOUBI

Major Professor: S. SONNY KIM
Committee: J. JAMES YANG
MI GEUM CHORZEPA
STEPHAN A DURHAM
IN KEE KIM

Electronic Version Approved:

Ron Walcott
Vice Provost for Graduate Education and Dean of the Graduate School
The University of Georgia
August 2022

تقدیم به ارزشمندترین دارایی های زندگیم؛ خانواده عزیزم به پاس محبت های بی دریغشان

ACKNOWLEDGMENTS

Many people helped me along the way with this dissertation. First, I would like to sincerely thank my advisor, Dr. Sung-Hee Sonny Kim, for his support, knowledge, and encouragement. His mentorship to give me the opportunity to work on research topics that I have been passionate about and providing me with the chance to work with an interdisciplinary research group. I would also like to truly appreciate Dr. Jidong Yang for his support, guidance, and willingness to offer help whenever I needed that during my Ph.D. Many thanks to Dr. Mi Geum Chorzepa for her being mentally supportive by encouraging me to stay happy during these challenging years. I also thank her for all she did to get project data from vendors. I am grateful to Dr. Stephan A. Durham for giving me insightful advice and for always being mentally supportive and willing to offer help. Moreover, I want to thank Dr. In kee Kim from the computer science department; for his support by either providing their local GPU or involving his master's student, Jai Rathore, in the project. I want to acknowledge this study's financial support from the Georgia Department of Transportation in the United States.

Thank you to all my friends and colleagues at UGA who helped me on this journey. Above all, I want to deeply appreciate my beloved parents and dearest siblings for all their ever-present love, encouragement, patience, and support throughout my academic career. I owe thanks to a very special person, my husband, Navid, for his continued and true love, support, and understanding during my pursuit of the Ph.D. degree. I could not have done this without you.

TABLE OF CONTENTS

Page

ACKNOWLEDGMENTS v

LIST OF TABLES x

LIST OF FIGURES xii

CHAPTERS

1. INTRODUCTION 1

1.1 BACKGROUND 1

1.2 RESEARCH OBJECTIVES 5

2. TRUCK TRAFFIC ASSESSMENT USING WIM DATA AND MACHINE LEARNING TECHNIQUES 6

2.1 PROBLEM STATEMENT 6

2.2 WEIGH-IN-MOTION TECHNOLOGY FOR TRAFFIC ASSESSMENT 6

2.2.1 TYES OF WIM SENSORS 7

2.3 WIM DATA ANALYSIS 8

2.4 MISSING AND ERRONEOUS DATA 10

2.5 QUALITY CONTROL CHECKS 11

2.6 DATA ACQUISITION 12

2.6.1 PROPERTIES OF GEORGIA WIM SITES 12

2.6.2 INACTIVE WIM STATIONS 13

2.6.3 WIM DATA QUALITY CONTROL 13

2.6.4 WIM DATA AFTER QC CHECKS 14

2.7 DEVELOPMENT OF STATE-SPECIFIC TRUCK TRAFFIC CLASSIFICATION GROUPS 15

2.7.1 TRAFFIC INPUTS IN AASHTO MEPDG MOP 17

2.7.1.1 VEHICLE CLASS DISTRIBUTION 18

2.7.1.2 MONTHLY DISTRIBUTION FACTOR 18

2.7.1.3 HOURLY DISTRIBUTION FACTOR 18

2.7.1.4 AXLES PER TRUCK CLASS 18

2.7.1.5 NORMALIZED AXLE LOAD SPECTRA (NALS) 19

2.8 MACHINE LEARNING TECHNIQUES 19

2.8.1 PRINCIPAL COMPONENT ANALYSIS 20

2.8.2 CLUSTERING TECHNIQUE 22

2.9 PAVEMENT PERFORMANCE ANALYSIS RESULTS 26

3. DEVELOPMENT OF LANE DISTRIBUTION FACTORS FOR GEORGIA USING WIM AND CCS DATA 32

3.1 PROBLEM STATEMENT 32

3.2 LANE DISTRIBUTION FACTOR 32

3.3 LITERATURE REVIEW 35

3.4 TRAFFIC DATA COLLECTION 36

3.4.1 WIM SITES 36

3.4.2 CCS SITES 37

3.5 DATA ANALYSIS 37

3.6 ESTIMATING LANE DISTRIBUTION FACTOR 42

3.7 RESULTS 45

3.8 CONCLUSION 48

4. REMOTE SENSING TECHNIQUES FOR PAVEMENT MAINTENANCE SCHEDULING PURPOSES 50

4.1 REMOTE SENSING METHODOLOGIES IN PAVEMENT ASSESSMENT 50

4.2 LITERATURE REVIEW 54

4.3 REMOTE SENSING PLATFORMS 55

  4.3.1 AIRPLANE 56

  4.3.2 UNMANNED AERIAL VEHICLE (UAV) 56

  4.3.3 VEHICLE 57

  4.3.4 SATELLITE 57

4.4 DATA ACQUISITION 58

  4.4.1 SENTINEL-2 SATELLITE 59

  4.4.2 PALNETSCOPE IMAGERY 60

4.5 DATA ANALYSIS 61

4.6 DISCUSSION 64

5. A DEEP LEARNING APPROACH FOR PAVEMENT CRACK IDENTIFICATION PURPOSES 66

5.1 PROBLEM STATEMENT 66

5.2 MACHINE LEARNING METHODOLOGIES IN PAVEMENT ASSESSMENT 67

5.3 PAVEMENT CRACK IDENTIFICATION NETWORK USING SEGNET ARCHITECTURE 69

5.4 DATASET COLLECTION AND PREPARATION 72

5.5 EXPERIMENTAL ENVIRONMENT 74

5.6 PERFORMANCE EVALUATION 75

5.7 RESULTS 76

6. CONCLUSIONS AND RECOMMENDATIONS 80

6.1 CONCLUSIONS 80

6.2 FUTURE WORK AND RECOMMENDATIONS 81

REFERENCES 82

LIST OF TABLES

Page

Table 1 – GDOT QC rules for WIM sites.. 11

Table 2 – Percent of variance explained by feature categories.. 22

Table 3 – Loading factors of 20 lower-level PCs. 24

Table 4 – Comparison of root mean squared differences between the clusters and TTCs.......... 27

Table 5 – Lane distribution factors by facility type.. 34

Table 6 – Lane distribution factors for multilane highways... 34

Table 7 – Description of variables.. 39

Table 8 – Model A- Estimating LDFs for the outermost lane... 43

Table 9 – Model B- Estimating LDFs for the second outermost lane 43

Table 10 – Simplified model A.. 44

Table 11 – Simplified model B 44

Table 12 – Updated Lane distribution factors for multilane highways 45

Table 13 – Updated lane distibution factors for multilane highways (Urban Interstate/Freeways/Expressways) 46

Table 14 – Updated lane distibution factors for multilane highways (Rural Interstate/Freeways/Expressways) 46

Table 15 – Updated lane distibution factors for multilane highways (Urban others)................... 47

Table 16 – Updated lane distibution factors for multilane highways (Rural others).................... 47

Table 17 – Measured IRI values for different pavement sections 63

Table 18 – Performance evaluation metrics.. 79

Table 19 – Pixel-level information of pavement cracks 79

LIST OF FIGURES

Page

Figure 1 – Flowchart of the dissertation 3

Figure 2 – Line graph. Vehicle class distribution by month, Site 185-0227 NB........................... 9

Figure 3 – Line graph. Vehicle class distribution by month, Site 185-0227 SB.. 9

Figure 4 – Line graph. GVW frequency distribution, Site 185-0227 10

Figure 5 – Screenshot. Inactive WIM stations in TADA.. 13

Figure 6 – Line graph. Monthly distribution factors, Site 185-0227 NB. 14

Figure 7 – Line graph. Monthly distribution factors, Site 185-0227 SB. 14

Figure 8 – Line graph. GVW frequency distribution, Site 185-0227. 15

Figure 9 – Line graph. Truck Traffic Classification groups based on National Cooperative Highway Research Program (NCHRP) project 1-37A. 16

Figure 10 – Bar graph. Determining the optimal number of the principal components for the attributes 21

Figure 11 – Line graph. Elbow method for determining K. 23

Figure 12 – Illustration. Nested PCA procedure. 24

Figure 13 – Plot. Clustering result and loading vectors... 25

Figure 14 – Map. Clusters of WIM sites. 26

Figure 15 – Line graph. Traffic pattern comparison of clusters and default TTC groups............ 28

Figure 16 – Line graph. JPCP pavement performance comparison of cluster-based traffic inputs and default TTC groups 30

Figure 17 – Line graph. Flexible pavement performance comparison of cluster-based traffic inputs and default TTC groups 31
Figure 18 – Map. Locations of active CCS and WIM sites in Georgia 38
Figure 19 – Bar chart. Satatewide traffic by year 40
Figure 20 – Bar chart. Statewide LDFs by year 41
Figure 21 – Aging process of asphalt pavement over time........ 51
Figure 22 – Line graph. Spectral variation of asphalt pavement by aging 52
Figure 23 – Line graph. Spectral variation of asphalt pavement by structural damage........ 52
Figure 24 – Pixels and their corresponding brightness values of a satellite image. 58
Figure 25 – Sentinel-2 satellite data acquisition.. 59
Figure 26 – PlanetScope imagery data acquisition. 60
Figure 27 – Spectral characteristics of Georgia pavement raods in Sentinel-2 satellite images. . 62
Figure 28 – Mixed pixel issue of Sentinel-2 images........ 63
Figure 29 – Spectrum value extraction using the SNAP software........ 64
Figure 30 – UGA GPR van. 73
Figure 31 – UGA road survey control units........ 73
Figure 32 – Sample image taken from the Georgia roads. 74
Figure 33 – Test images after 10 epochs 77
Figure 34 – Test images after 50 epochs 78
Figure 35 – Test images after 100 epochs 78

CHAPTER 1

1. INTRODUCTION

This chapter presents the background information and objectives in this study.

1.1 Background

Pavement Management is a continuous and ongoing activity that is always accompanied by transportation engineering and should satisfy the needs of a given pavement to prevent failure and extend the pavement life as well as taking potential materials or techniques to improve the existing road facilities. Pavement management is generally categorized into two levels: network level and project level. The network-level pavement management is the summary of information related to the entire highway network applied for large groups of projects. However, project-level pavement management relates to more technical and specific pavement section decisions (Peterson, 1987).

In terms of pavement assessment, the visual survey is a simple and traditional method for collecting distress information about the pavement surface. The Distress Identification Manual (DIM) for the Long-Term Pavement Performance (LTPP) Program is the primary guide for all distress surveys (Miller and Bellinger, 2003). Since road networks in the U.S. are so extensive, it is not feasible to use traditional approaches in surveying all existing roadways for their rideability and structural integrity. In addition to the difficulties associated with creating a comprehensive evaluation of thousands of miles, other factors also restrict the comprehensive road evaluation. Some of these limiting factors are time (road needs to be closed off during inspections causing traffic flow disruption), hazards for inspectors on highways, and the need for trained/experienced inspectors.

Most Department of Transportation (DOT) agencies perform routine inspections on their infrastructures in cycles of one to three years. The state-of-the-art remote sensing and machine learning technologies offer tools to replace or complement existing traditional methods. They can serve many needs of transportation engineers in DOTs to assist with the routine inspections of roads and bridges (Ozden et al., 2016). Recently, transportation agencies nationwide have incorporated remote sensing approaches into their standard specifications for the pavement management system (Schnebele et al., 2015) since it is an accurate, robust, and fast technique to collect data and is considered an efficient approach for pavement assessment in network level.

This study attempts to employ Weigh-In-Motion (WIM) and Continuous Count Stations (CCS) technology, remote sensing techniques, and state-of-the-art machine learning methodologies for transport infrastructure monitoring in Georgia. Figure 1 illustrates the connection between different topics conducted in this dissertation which generally focuses on pavement management through the lens of design and maintenance. In this study, two research projects are performed on pavement design. Equivalent Single Axle Load (ESAL) factors and Pavement Mechanistic-Empirical Design (PMED) traffic inputs are updated using a large dataset obtained from WIM sensors. In addition, state-specific Truck Traffic Classification (TTC) groups are developed using WIM data. In terms of pavement design, another study is conducted to update the Lane Distribution Factors (LDF) using WIM and CCS data in support of Georgia's pavement design manual. The other two projects are related to the pavement maintenance category. First, the application of remote sensing techniques in pavement management is discussed. Two satellite imagery sources (Sentinel-2 and PlanetScope) are utilized to evaluate their capability in observing transportation infrastructure conditions. Finally, deep learning methods are discussed to investigate the usefulness of state-of-the-art image processing techniques in pavement surface health monitoring. These two projects aim to predict the roadway segments' distress condition and to see how well the pavement distress condition can be estimated from freely accessible satellite images and the newly developed deep learning architectures. The novelty of the study is utilizing a vehicle (UGA's GPR scan van) primarily used for another purpose to overcome the shortcomings of the satellite remote sensing technology. The combination of this work aids in mapping the available data sources, analytics, and implementation of the results for improving pavement management practice for Georgia. The specific aims of this dissertation are listed below and discussed in detail in each chapter.

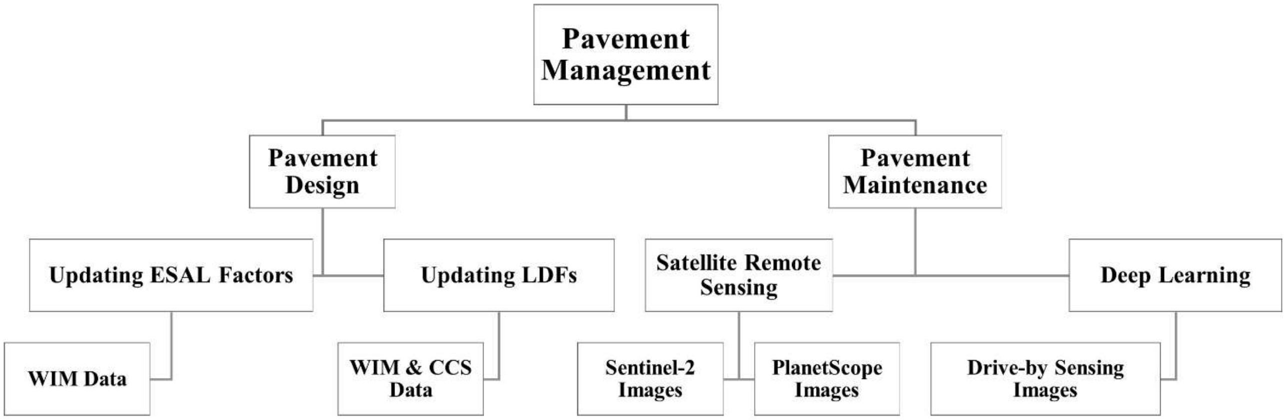

Figure 1. Flowchart of the dissertation.

Chapter 1 aims to:

1. Discuss background information and provide the perspective of the approaches taken in this study.

Chapter 2 aims to:

1. Provide background information about WIM technology, properties of WIM stations in Georgia and their capabilities in providing traffic information for pavement assessment.
2. Develop Python codes to generate MEPDG traffic inputs using WIM data.
3. Develop state specific TTC groups using machine learning techniques to facilitate the application of MEPDG software in Georgia.

Chapter 3 aims to:

1. Provide background information about the lane distribution factors currently adopted in the Georgia pavement design manual.
2. Develop Python codes to update lane distribution factors using WIM and CCS data.
3. Develop models using statistical methods to facilitate the application of updated lane distribution factors using the most recent traffic data.

Chapter 4 aims to:

1. Discuss the remote sensing technology and its application in pavement management.
2. Employ remote sensing satellite imagery to extract the spectrum features of asphalt pavement sections with cracks and distresses.
3. Perform time series analysis to predict the pavement distresses on-time for scheduling cost-effective maintenance works.

Chapter 5 aims to:

1. Review the state-of-the-art advancements and technologies in the field of machine learning and image processing for pavement crack identification purposes.
2. Employ a newly developed semantic segmentation model for pavement crack identification.
3. Determine how well the fine-tuned deep learning-based algorithm performs in terms of pavement crack identification.

Finally, Chapter 6 provides conclusions and recommendations for future studies.

1.2 Research Objectives

The primary objectives of this study are:

- To utilize WIM technology for traffic and pavement assessment purposes.
- To generate the state specific TTC groups to facilitate the adoption of the MEPDG in Georgia.
- To update lane distribution factors for the Georgia pavement design manual using the most recent WIM and CCS data.
- To leverage freely available satellite images to predict pavements distress situation.
- To predict the pavement distress severity using a deep learning-based algorithm.
- To maintain the resilient infrastructures using the recent advancements in developing technologies.

CHAPTER 2

2. TRUCK TRAFFIC ASSESSMENT USING WIM DATA AND MACHINE LEARNING TECHNIQUES

2.1 Problem statement

The pavement Mechanistic-Empirical (ME) design requires high-dimensional traffic feature inputs by categories, including Vehicle Class Distributions (VCD), Monthly Distribution Factors (MDF), Hourly Distribution Factors (HDF), and Normalized Axles Load Spectra (NALS). In simplifying the Pavement ME design practice, Truck Traffic Classification (TTC) groups are commonly used for characterizing traffic inputs. Thus, properly defining TTC groups is critical for state-specific pavement ME design practice. In this study, the truck traffic data from existing Weight-in-Motion (WIM) stations were mined to develop specific TTC groups to assist with pavement ME design practice in Georgia. An effective data analytics procedure was developed by leveraging unsupervised machine learning techniques to reduce the high-dimensional traffic features by stratified Principal Component Analysis (PCA), followed by K-means clustering to establish appropriate TTC groups. For a case study, the performance of two typical designs was evaluated using the AASHTOWare pavement mechanistic-empirical (ME) design software with respect to two scenarios of traffic inputs: (1) the derived cluster-based groups, and (2) the national default TTC groups.

2.2 Weigh-In-Motion Technology for Traffic Assessment

The WIM technology, using sensors embedded in pavement, has enabled continuous collection of high-resolution vehicle class and axle weight data, such as gross vehicle weights, axle configurations and weights, axle spacings, vehicle classifications, and speeds. The WIM data are used for various purposes, including the design of pavements or bridges, highway planning, motor vehicle enforcement, and legislative/regulatory studies (FHWA 2018). Based on Georgia's Traffic Monitoring Guide (Wiegand, 2018) published by GDOT, the GDOT Office of Transportation Data (OTD) collects WIM data at 14 permanent continuous count stations (CCSs) and approximately 35 portable sites located throughout Georgia. WIM technology helps to collect traffic loading–related information, such as vehicle counts, axle and gross weights, vehicle classification, etc. It allows for continuous data acquisition and provides an accurate representation of actual traffic loadings on Georgia's highways.

The main components of WIM systems include:

(1) WIM sensor embedded in the roadway surface or under a bridge deck to detect, weigh, and classify vehicles. A sensor array is the combination of WIM sensor and loop detectors within a weighing lane.

(2) Electronics to control system functions, process sensor outputs, and provide recorded information for display and storage.

(3) Infrastructure, including conduit, bore, cabinet, poles, and junction boxes.

(4) Support devices to power the WIM electronics and communication devices to transmit the collected data to a remote server.

(5) Software installed in the WIM electronics to process sensor measurements, analyze, format, and store collected data (FHWA 2018).

2.2.1 Types of WIM Sensors

Several types of in-road WIM sensors are available, but the most frequently used types include bending plate, load cell, quartz piezo, polymer piezo, and the strain gauge strip sensor. Wide sensors, such as bending plate and load cell, provide the opportunity for the tire to rest fully on the sensor, while other sensors, referred to as narrow or strip sensors, meet only a part of the tire footprint as a vehicle moves over them. The available sensors have a broad range in accuracy and cost that should be considered during the sensor selection process. If high-accuracy weight data collection over a long period of time is required, then either a load cell or bending plate sensor would be the preferred solution. In terms of life cycle costs, the bending plate and load cell sensors are more cost effective in comparison with piezo sensors with high data quality if properly maintained/calibrated. The polymer piezo sensors are sensitive to temperature fluctuations and pavement stiffness due to seasonal changes; thus, these sensors must be calibrated every 6 to 12 months to keep accuracy in weight measurements. In summary, for projects with a typical life expectancy of 8 to 10 years, load cells or bending plate sensors would be preferred. Quartz piezo or strain gauge strip sensors typically have shorter lifespans of 3 to 5 years (FHWA 2018).

2.3 WIM Data Analysis

Different Python codes were developed to analyze the raw WIM data. First, the vehicle class distribution of directional WIM stations was visualized. Figure 2 and Figure 3 show the vehicle class distribution by month for north- and southbound directions of WIM station 185-0227, respectively. As seen in the figures, the class 9 vehicle is the most dominant truck for all the WIM stations throughout the year. Moreover, Figure 4 shows the GVW frequency distribution of WIM station 185-0227. Based on the figure, the first few weight ranges were considered outliers and were removed in the QC process to retrieve the real weight distribution of vehicles.

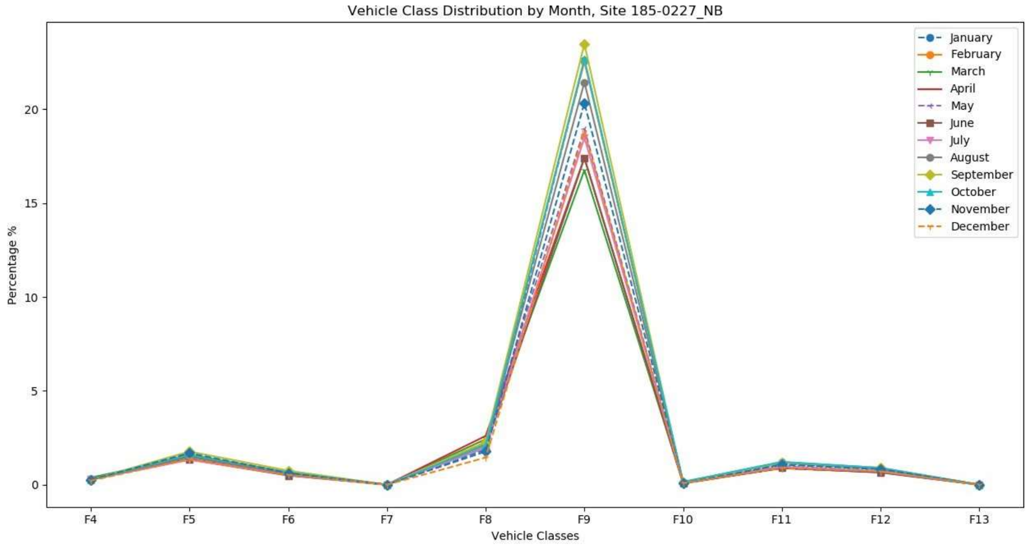

Figure 2. Line graph. Vehicle Class Distribution by month, Site 185-0227 NB.

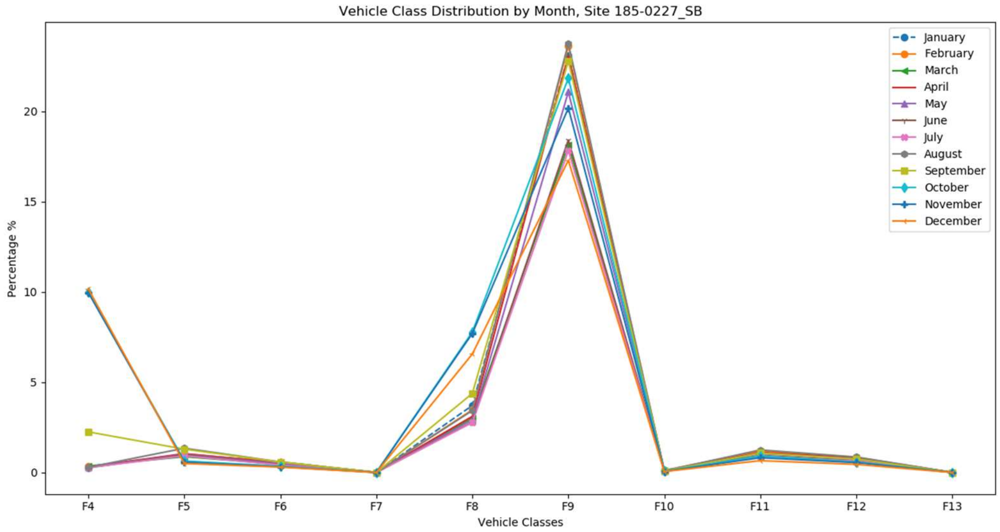

Figure 3. Line graph. Vehicle Class Distribution by month, Site 185-0227 SB.

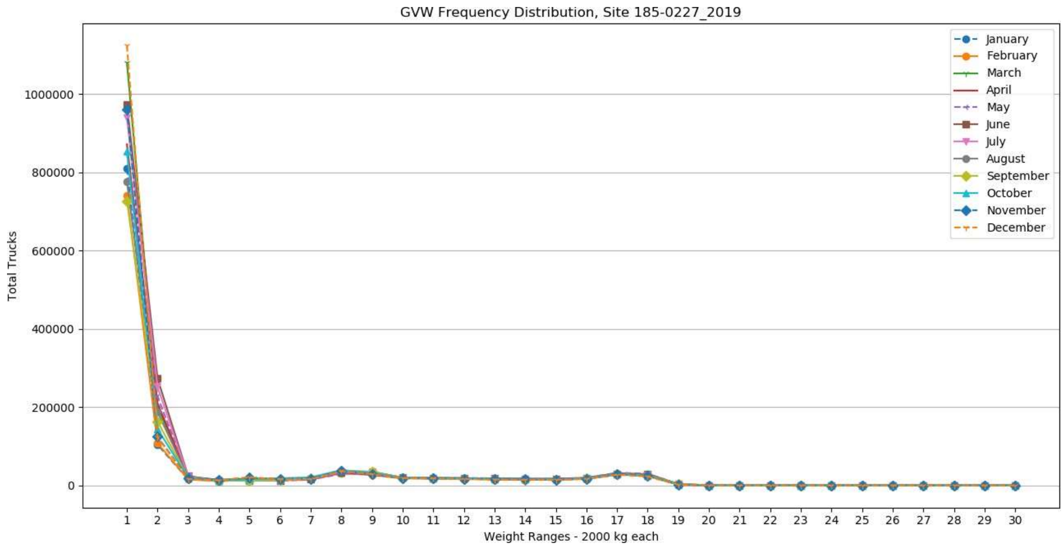

Figure 4. Line graph. GVW frequency distribution, Site 185-0227.

2.4 Missing and Erroneous Data

Generally, there are two quality issues with WIM data: missing values and erroneous data. Power outages or sensor malfunctions can cause missing values (Wei and Fricker 2003). A variety of other factors may affect WIM data quality, including environmental changes, pavement conditions, lack of calibration, and the type of WIM technology. Moreover, drivers' behavior, such as accelerating, decelerating, and weaving, also impact the data quality depending on the sensor technologies (Wei and Fricker 2003, Stone et al. 2011). In addressing the data quality issues in practice, state departments of transportation (DOTs) have developed standard quality control (QC) checks to ensure the quality of the data before releasing them for planning or design practice. To ensure the quality of WIM data used in the analysis in this project, the research team implemented a customized QC procedure derived from the QC policies currently used by GDOT (Wiegand 2018) and NCDOT (Stone et al. 2011).

2.5 Quality Control Checks

Based on previous studies, only 15–25 percent of the collected WIM data are considered good quality data due to lack of skilled staffing, resources, and support software. Thus, both the Traffic Monitoring Guide (FHWA 2016) and AASHTO Guidelines for Traffic Data Programs (AASHTO 2009) emphasize the QC requirements in traffic monitoring programs. The FHWA Long-Term Pavement Performance Program developed mandatory verification QC checks and software on the collected traffic data in the field before merging with the database. The GDOT Office of Transportation Data currently has a comprehensive quality control and quality assurance (QA) process in place. Table 1 shows GDOT's quality control rules for WIM sites (Wiegand, 2018).

Table 1. GDOT QC rules for WIM sites.

Quality Control Rule	Description	Data Type
Error Ratio	The system will reject the day(s) that have vehicles in class 15 (the error bin) greater than X percent of the total volume.	Class
Minimum Class Hours	The system will reject data that do not provide a complete 24 hours of truck data.	Class
No Truck Data	The system will reject the day(s) if no truck data exist for the day.	Class
No Trucks Lane	The system will reject the data if there is no truck traffic in one lane for the day.	Class
Ratio of Class 1 to Class 2	The system will flag any day(s) for which the volume in vehicle class 1 (motorcycles) exceeds the volume in vehicle class 2 (cars).	Class
Ratio of Class 13 to Class 9	The system will flag any day(s) for which the volume in vehicle class 13 exceeds the volume in vehicle class 9.	Class
Ratio of Long Class to Short Class	The system will flag any day(s) for which the total of the volumes in vehicle classes, 11, 12, and 13 (long class) exceeds the volumes in vehicle classes 8, 9, and 10 (short class).	Class
Trucks Last Year	The system will reject any daily truck traffic volumes that are substantially different from the previous year.	Class
Zero Long Class	The system will reject day(s) for which the long truck classes have a zero volume.	Class
Zero Short Class	The system will reject day(s) for which the short truck classes have a zero volume.	Class

Minimum Hours	The system will reject any day that does not have data for every hour	Volume
No Data	The system will reject a day for which there are no data.	Volume
Volume Last Year	The system will reject any daily traffic volumes that are substantially different from the previous year.	Volume
Volume Split	The system will flag the entire set of counts if volume in one direction is over X percent of the total volume. This check is not applied to nondirectional data.	Volume
Volume Step	The system will reject the day(s) that show a sudden dramatic change in hourly volumes.	Volume
Volume Step Lane	The system will flag the day(s) that have a sudden dramatic change in hourly lane volumes.	Volume
Zero Hours All Day	The system will reject any day that has consecutive zero volumes for the entire day.	Volume
Zero Hours During Day	The system will reject any day that has consecutive zero volumes at any time during the day.	Volume
Zero Hours During the Night	The system will reject any day for which there are consecutive zero volumes at any time during the night.	Volume
Class 9 Average Steer Weight	The system will reject any day for which the Class 9 average steer weight is outside the parameters.	WIM
Class 9 BC Spacing	The system will reject any day for which the Class 9 average B–C axle spacing is outside the parameters.	WIM
Maximum Axle Count	The system will reject any day for which the ratio of vehicles to axles is more than X.	WIM
Maximum Wheelbase	The system will reject any day for which the wheelbase is more than X.	WIM
Minimum Axle Count	The system will reject any day for which the ratio of vehicles to axles is less than X.	WIM

2.6 Data Acquisition

2.6.1 Properties of Georgia WIM Sites

In Georgia, the vendor uses two WIM sensor models in the state's current WIM system: quartz and bending plate sensors. Lanes instrumented with quartz sensors provide information on both vehicle weight and class. Although bending plate sensors also record vehicle class and weight data simultaneously, the vendor considers the weight data from quartz sensors to be more accurate and reliable (Chorzepa et al., 2020).

2.6.2 Inactive WIM Stations

GDOT uses the Traffic Analysis and Data Application (TADA), a web application, to disseminate traffic data collected from the Georgia Traffic Monitoring Program. The application utilizes a dynamic mapping interface that allows users to access data from the map in a variety of reports, graphs, and data formats. Historical data from two inactive WIM stations, 245-0218 and 143-0126, were evaluated. The 245-0218 WIM data (Figure 5) are erroneous and incomplete. Figure 5 shows a screenshot of TADA in which the details of one of the inactive WIM stations are characterized.

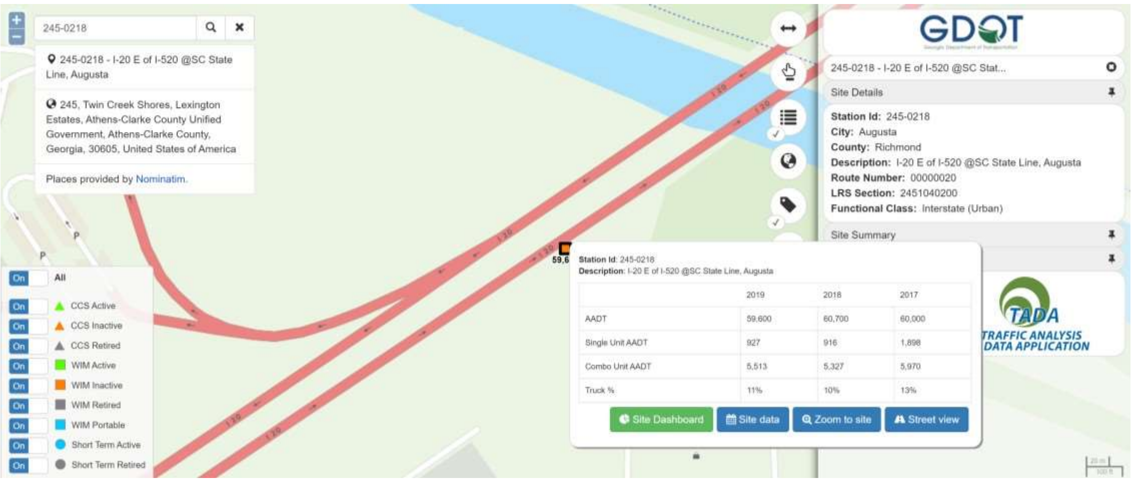

Station Id: 245-0218
City: Augusta
County: Richmond
Description: I-20 E of I-520 @SC State Line, Augusta
Route Number: 00000020
LRS Section: 2451040200
Functional Class: Interstate (Urban)

Station Id: 245-0218
Description: I-20 E of I-520 @SC State Line, Augusta

	2019	2018	2017
AADT	59,600	60,700	60,000
Single Unit AADT	927	916	1,898
Combo Unit AADT	5,513	5,327	5,970
Truck %	11%	10%	13%

Figure 5. Screenshot. Inactive WIM stations in TADA[1].

2.6.3 WIM Data Quality Control

The North Carolina DOT and GDOT QC criteria were applied to Georgia's raw WIM data to process data and generate AASHTOWare Pavement ME Design traffic inputs.

---

[1] https://gdottrafficdata.drakewell.com/publicmultinodemap.asp

2.6.4 WIM Data After QC Checks

Figure 6 and Figure 7 show the monthly distribution factors of the directional WIM stations after applying the QC criteria. Furthermore, Figure 8 illustrates the GVW frequency distribution for site 185-0227 after QC checks.

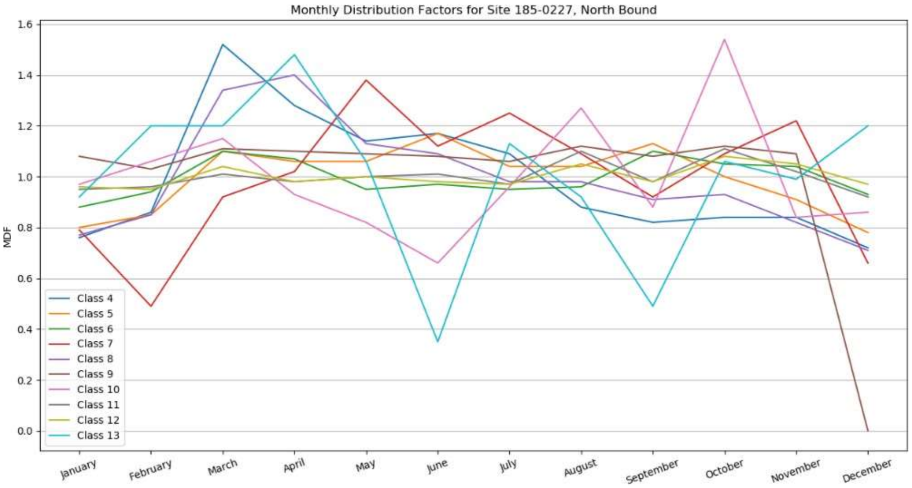

Figure 6. Line graph. Monthly Distribution Factors, Site 185-0227 NB.

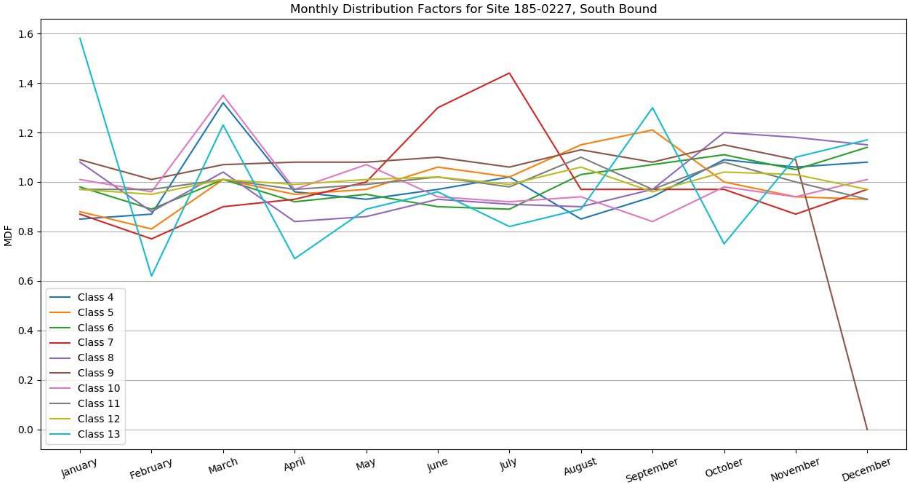

Figure 7. Line graph. Monthly Distribution Factors, Site 185-0227 SB.

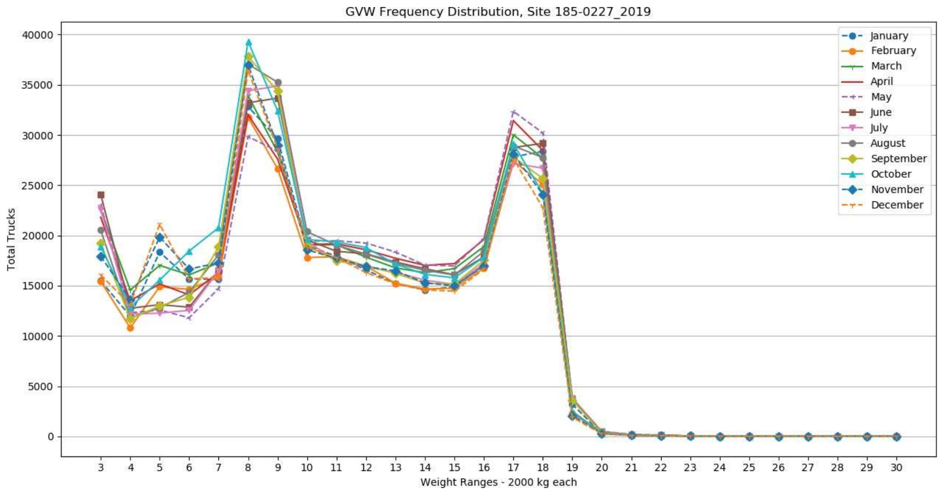

Figure 8. Line graph. GVW frequency distribution, Site 185-0227.

The compiled WIM data include five feature categories consistent with the AASHTOWare Pavement ME Design traffic inputs: (1) Vehicle Class Distribution (VCD) factors, (2) Monthly Distribution Factors (MDFs) for each vehicle class, (3) Hourly Distribution Factors (HDFs) for each hour of the day, (4) Normalized Axle Load Spectra (NALS) for single-axle loads across vehicle classes and weight bins, and (5) NALS for tandem-axle loads across vehicle classes and weight bins. In compiling WIM data in AASHTOWare Pavement ME Design traffic input format, the tridem- and quad-axle load spectra were generally excluded from the analysis since pavement designs are less sensitive to tridem and quad axles due to their low impact and representation as compared to single- and tandem-axle load applications (Selezneva et al. 2016). As a result, a total of 564 design-related traffic features were obtained for each WIM site, including 10 VCD features, 120 MDF features, 24 HDF features, 230 NALS – single-axle features, and 180 NALS – tandem-axle features.

2.7 Development of State-Specific Truck Traffic Classification Groups

Truck traffic classification (TTC) groups were originally developed based on the LTPP databases and provide the opportunity for engineers to use the national default values (i.e., Level 3 design inputs) when site-specific traffic data are not available. Seventeen TTC groups were defined based on the distributions of vehicle classes in traffic streams (ARA 2004), as shown in Figure 9. In the PMED process, one typically obtains traffic composition on a specific roadway section from short-term traffic counts to identify the closely matched TTC group. Then, the required design traffic inputs associated with the identified TTC group can be obtained from the historical databases (Wang et al. 2015). However, the actual traffic data may not match well with any of the national default TTC groups. Thus, using the closely matched TTC group for design may result in over- or under-design of pavement structure. Nassiri et al. (2014) investigated the influence of site-specific traffic characteristics and the AASHTOWare Pavement ME Design default values on the performance of both flexible and rigid pavements in Alberta. Based on the results, TTC groups were found to be influential on AC pavement performance, especially for rutting. In another study, Li et al. (2015) aimed at developing simplified TTC groups based on cluster analysis of vehicle class distributions in Arkansas. Like many other states in the U.S., Georgia currently uses national default values (Level 3 design inputs) for pavement design.

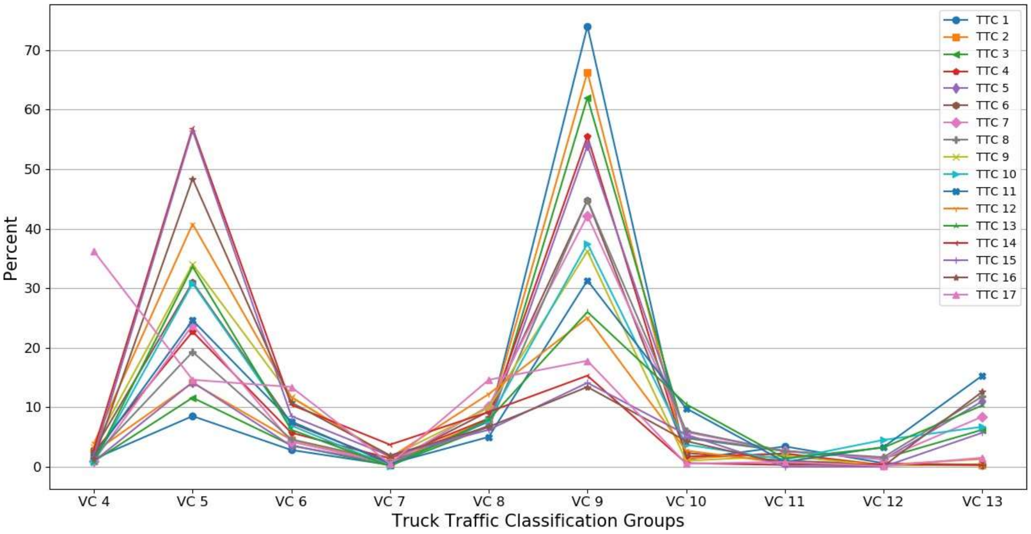

Figure 9. Line graph. Truck Traffic Classification groups based on National Cooperative Highway Research Program (NCHRP) Project 1-37A (Ara, Inc. 2004).

The purpose is to develop customized or state specific TTC groups using existing WIM data in Georgia. We aimed to leverage unsupervised machine learning techniques to develop clusters (groups) of truck traffic by mining the comprehensive WIM data compiled in the AASHTOWare Pavement ME Design traffic input formats by categories, including VCD, MDF, HDF, and NALS.

2.7.1 Traffic Inputs in AASHTO MEPDG MOP

The AASHTO MEPDG MOP requires various data to design new or rehabilitated pavement structures. Generally, there are four different categories of inputs in AASHTOWare Pavement ME Design software (PMED). These input data are climate inputs, layer/material property inputs, design features and layer property inputs, and traffic inputs. The required traffic input data which can be extracted from WIM data are: VCDs, MDFs, HDFs, axles per truck class, and axle load distribution factors or NALS. For each of these traffic inputs, depending on the level of design, the PMED requires traffic distributions for each of 10 standard FHWA vehicle classes (i.e., classes 4 through 13). The design levels are defined as follows:

- Level 1: Most accurate design level requiring site-specific weight and volume data collected at or near the project site.
- Level 2: Intermediate accuracy design level with modest knowledge of traffic characteristics requiring regional weight data and site-specific volume data.
- Level 3: Least accurate design level with knowledge only of statewide default weight and volume data.

In the following sections, the five different traffic input data are defined separately.

2.7.1.1 Vehicle Class Distribution

VCD represents the percentage of each truck class (i.e., 4 through 13) within the annual average daily truck traffic (AADTT) for the base year, which is defined as the first year of the forecast period. The sum of the percent AADTT of all truck classes must equal 100.

2.7.1.2 Monthly Distribution Factor

MDF is defined as the seasonal differences in AADTT by allocating a normalized weight factor to each month of the year. As the default, a seasonally independent value of 1 for each of the 12 months is assumed as level 3 data. In this way, months with higher AADTT will receive a weight factor greater than 1, whereas months with lower AADTT will receive a factor less than 1 (ARA, Inc. 2004). The sum of the MDF of all truck classes must equal 12.

2.7.1.3 Hourly Distribution Factor

HDF is defined as the percentage of total trucks within each hour using data measured continuously over a 24-hour period. The sum of the percent of daily truck traffic per time increment should add up to 100 percent.

2.7.1.4 Axles per Truck Class

This input represents the average number of axles for each truck class (i.e., 4 to 13) for each axle group type (i.e., single, tandem, tridem, and quad).

2.7.1.5 Normalized Axle Load Spectra (NALS)

The axle load distribution factors represent the percentage of the total axle applications for load intervals in a specific axle group type (i.e., single, tandem, tridem, and quad) and vehicle classes 4 through 13. The load intervals for each axle group type are as below:

- Single axles – 3,000 lb to 40,000 lb at 1,000-lb intervals.
- Tandem axles – 6,000 lb to 80,000 lb at 2,000-lb intervals.
- Tridem and quad axles – 12,000 lb to 102,000 lb at 3,000-lb intervals.

The NALS can only be extracted from WIM data. Thus, the level of input depends on the data source (i.e., site, regional, or national). To generate AASHTOWare Pavement ME Design traffic inputs, the WIM volume and weight data were reviewed using a quality control procedure. The cleaned data were then processed using computer programming to generate traffic inputs, including VCD, MDF, HDF, axles per truck class, and NALS.

2.8 Machine Learning Techniques

Since obtaining high-quality WIM data is an expensive and time-consuming process, not all roads are equipped with WIM sensors. As a result, site-specific traffic data are limited to specific road sections. The issue appears when designing new pavements since designers have no idea about the TTC grouping of the section, subsequently leading to confusion in the selection of PMED input data. Machine learning methodologies in transportation engineering have been widely used in recent years. One common approach is clustering WIM stations to generate similar traffic-loading spectra as well as traffic data for designing new road sections without site-specific traffic information. Generally, the traffic vehicle class distribution has been utilized as a feature for clustering WIM stations.

In this study, VCD, MDF, HDF, and NALS for single- and tandem-axle loads were generated and used as features for clustering analysis. Therefore, the purpose of this study was to find the trucking pattern of the Georgia roads based on PMED traffic input data and generate new TTCs to determine whether, apart from VCD, other input data play a considerable role in clustering WIM sites.

2.8.1 Principal Component Analysis

Principal component analysis (PCA) is an unsupervised method that is commonly used for dimension reduction, in which high-dimensional features are projected to a low-dimensional space without losing much information. Principal Components (PCs) are created in the order of the amount of the variation and are orthogonal to each other. In other words, PC1 captures the direction of most variance, PC2 is orthogonal to PC1 and captures the direction of second most variation, and so forth. As discussed previously, PCA is applied to each feature category separately. Figure 10 shows the top 10 PCs for each of 5 feature categories defined previously.

As seen in Figure 10, the variance captured by each subsequent PC decreases. The number of PCs (i.e., dimensions) to keep is a judgment call that reflects the trade-off between the amount of variance to retain and the complexity (dimensionality) of the resulting feature space. For this analysis, the decision was based on the sudden drop of variance as well as retaining at least 60 percent of variances for each feature category. The ultimately retained PCs are indicated in the red rectangle in Figure 10, and the corresponding percentages of variance captured are summarized in Table 2. As a result, a total of 20 PCs (i.e., three PCs each for VCD, MDF, and HDF, respectively; six PCs for NALS-Single Axles; five PCs for NALS-Tandem Axles) were retained, which is a significant reduction from the original 565 features. The 20 PCs were used for the subsequent cluster analysis.

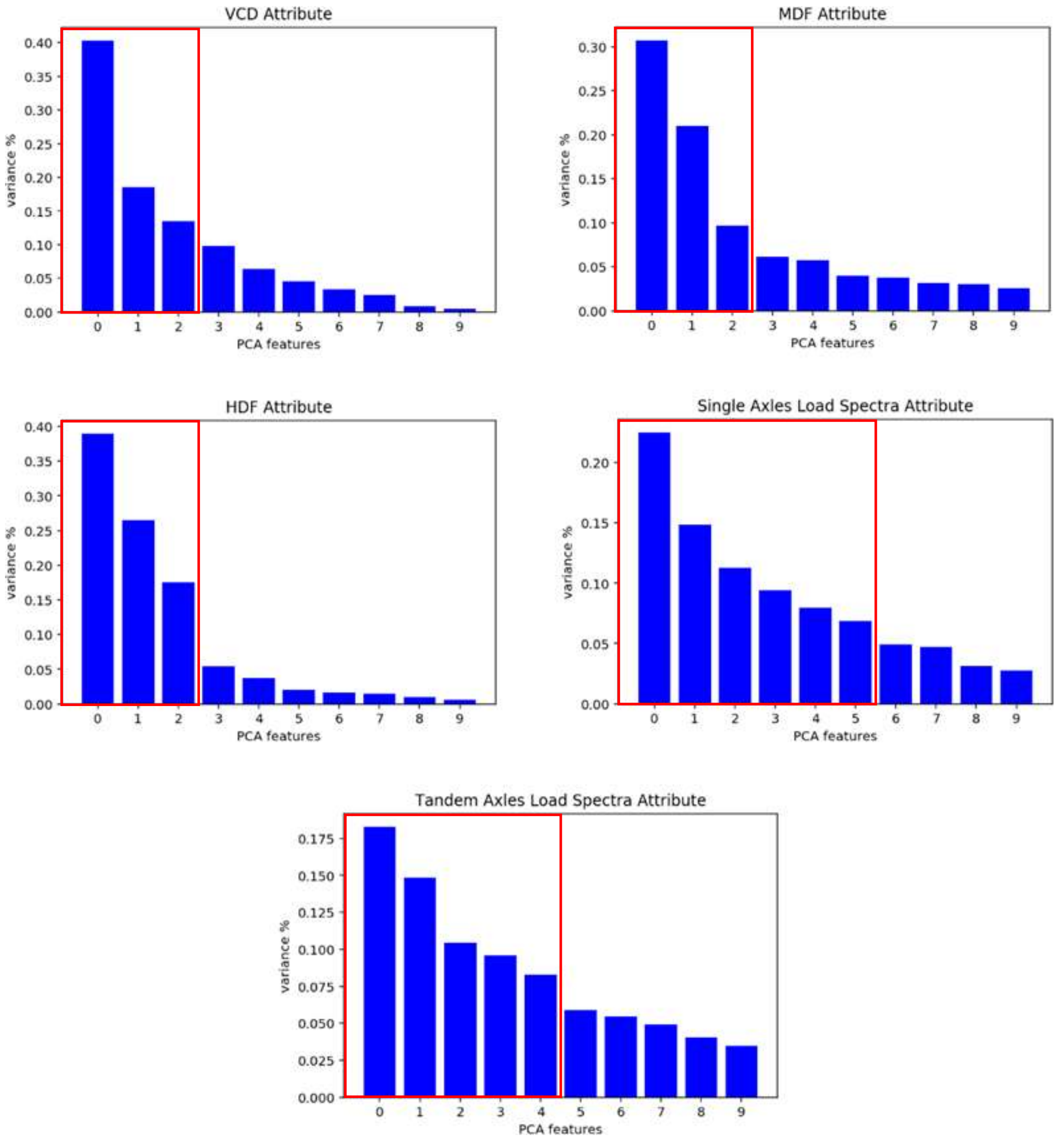

Figure 10. Bar graph. Determining the optimal number of principal components for the attributes.

Table 2. Percent of variance explained by feature categories.

Feature Category	Principal Component (PC)						Total
	PC1	PC2	PC3	PC4	PC5	PC6	
VCD	0.41	0.19	0.14	▨	▨	▨	0.74
MDF	0.30	0.21	0.09	▨	▨	▨	0.60
HDF	0.40	0.27	0.18	▨	▨	▨	0.85
NALS-Single Axles	0.22	0.14	0.11	0.09	0.08	0.06	0.70
NALS-Tandem Axles	0.18	0.15	0.10	0.09	0.08	▨	0.60

Shading denotes “Not Used”.

2.8.2 Clustering Technique

Cluster analysis aims to find homogeneous subgroups among observations such that the observations within one group will be similar to one another and different from the objects in other groups. A variety of cluster methods have been developed with K-means being the most popular one that works well with many different data sets. In K-means clustering, the number of clusters, K, needs to be prespecified. The idea behind the K-means method is to find the K clusters so that the within-cluster variation is minimized. With the commonly used Euclidean distance as the proximity measure, the K-means algorithm can be expressed as an optimization problem as in equation 1.

$$\underset{C_1,\ldots,C_k}{\text{minimize}}\left\{\sum_{k=1}^{K}\frac{1}{|C_k|}\sum_{i,i'\in C_k}\sum_{j=1}^{p}\left(x_{ij}-x_{i'j}\right)^2\right\} \qquad (1)$$

Where,

xij = the jth feature of observation i p = the number of features

$|Ck|$ = the number of observations in the kth cluster

The within-cluster sum-of-squares is also referred to as inertia, which measures how internally coherent the clusters are. Inertia is commonly used to determine the optimal number of clusters (K). A range of K values were experimented within the PC features derived previously. The inertia was then plotted against K in Figure 11, showing the inertia reduces as K increases. In extreme cases when the number of observations equals K, the inertia reduces to zero. In practice, the elbow method is often applied, where K is chosen as the point of the maximum curvature in the inertia plot (indicated by the red arrow in Figure 10). Following this approach, K was chosen to be 4 in this study.

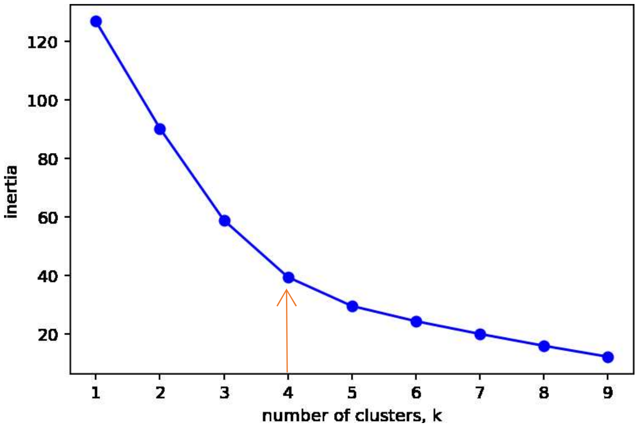

Figure 11. Line graph. Elbow method for determining K.

For visualization purposes, the 20 PCs derived previously (referred to as the lower-level PCA) were further projected onto a two-dimensional space again using the PCA method, referred to as the higher-level PCA. This allowed the researchers to visually inspect how the 20 WIM sites are clustered on a two-dimensional plane. This nested PCA procedure is illustrated in Figure 12.

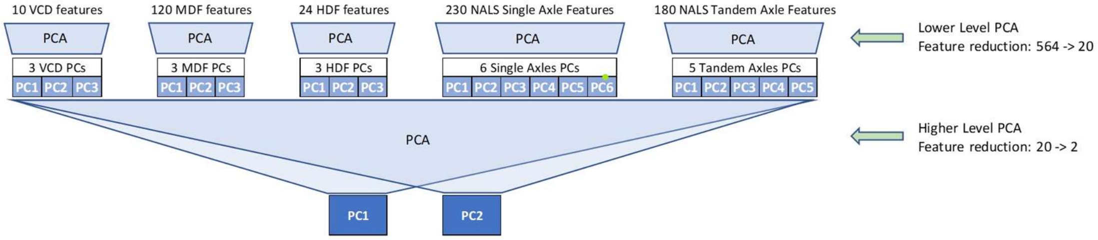

Figure 12. Illustration. Nested PCA procedure.

Corresponding to the higher-level PCA, the loading factors of the 20 lower-level PCs were calculated with respect to the two higher-level PC axes and are shown in Table 3.

Table 3. Loading factors of 20 lower-level PCs

Variables	PC1	PC2
PC2_Single_axles	-0.151155	-0.275597
PC2_VCD	-0.135996	-0.308707
PC2_MDF	-0.128659	0.191469
PC1_MDF	-0.050055	0.115607
PC3_Tandem_axles	-0.047125	0.012843
PC5_Single_axles	-0.019196	-0.093869
PC4_Single_axles	-0.010344	0.061058
PC3_VCD	-0.009486	-0.223399
PC3_HDF	0.010548	0.173314
PC2_HDF	0.025426	-0.308047
PC5_Tandem_axles	0.056787	-0.321616
PC1_Tandem_axles	0.181245	0.214771
PC1_Single_axles	0.201175	0.267167
PC6_Single_axles	0.242751	-0.330624
PC4_Tandem_axles	0.272299	-0.301626
PC3_Single_axles	0.280960	0.040971
PC2_Tandem_axles	0.348197	0.196957
PC1_HDF	0.360387	-0.236826
PC3_MDF	0.432520	0.237685
PC1_VCD	0.457495	-0.129976

The clusters of 20 WIM sites were plotted in the two-dimensional plane in the higher-level PC space, together with the scaled loading vectors, shown in Figure 13.

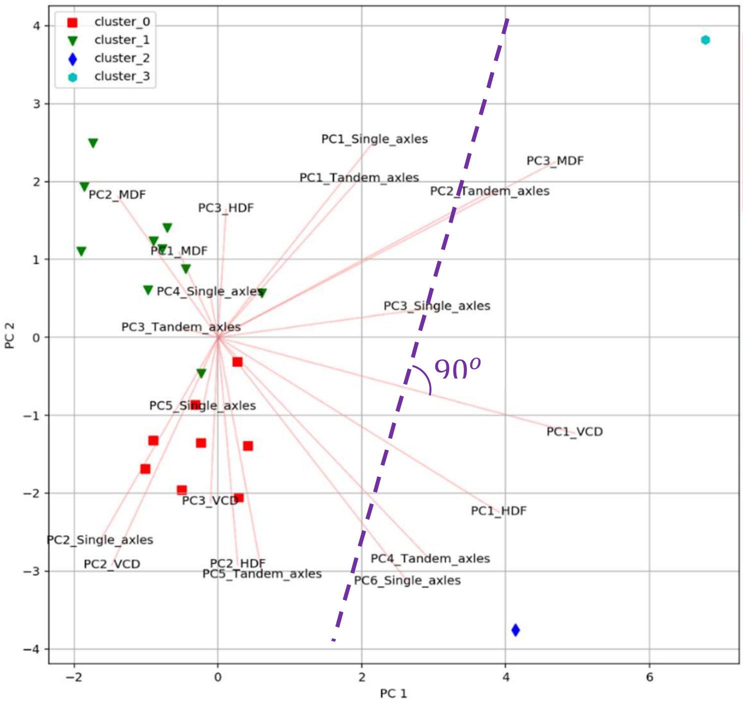

Site ID	Cluster
021-w334_NB	0
021-w334_SB	0
217-0218_EB	0
217-0218_WB	0
245-0218_EB	0
245-0218_WB	0
175-0247_EB	0
175-0247_WB	0
185-0227_NB	1
185-0227_SB	1
285-0243_NB	1
285-0243_SB	1
127-0312_NB	1
127-0312_SB	1
051-0387_NB	1
051-0387_SB	1
143-0126_EB	1
143-0126_WB	1
051-0368_EB	2
051-0368_WB	3

Figure 13. Plot. Clustering results and loading vectors.

As shown in Figure 13, all clusters are clearly separated in the two-dimensional higher-level PC space. Cluster 0 (red square) consists of 8 WIM sites, which are in the lower left region, while cluster 1 (green triangles) consists of 10 WIM sites, which are in the upper left region. Clusters 2 and 3 (blue diamond and cyan circle) contain only one WIM site each and both belong to the same WIM station 051-0368. For direct reference, the WIM site IDs, and their corresponding clusters are included in Figure 13, as well. Apparently, clusters 2 and 3 (representing directional traffic at the same WIM station: 051-0368) are further separated from other sites and they are also farther apart from each other in Figure 14. This seemingly strange clustering outcome is intuitively interpretable, as the station 051-0368 is located on Interstate 16 near the City of Savannah and serves as the gateway for heavy trucks entering and leaving the Savannah Port. The distinct directional patterns of truck traffic at this station are well expected. The lines in Figure 13 represent loading vectors for the 20 lower-level PCs. They can be used to interpret which features or feature categories have contributed to separating different clusters. For example, the VCD feature category (PC1_VCD) plays the most important role in separating clusters 2 and 3 from clusters 0 and 1. This can be seen from Figure 13 by drawing an imaginary line that is perpendicular to the PC1_VCD vector (see the dashed purple line). This is due to the fact that the vehicle class distribution at the station 051-0368 near the Savannah Port is quite different from other sites in Georgia. Besides PC1_VCD, other vectors, especially those crossing the dashed purple line (e.g., PC1-HDF, PC3-MDF, and PC2-tandem-axles, etc.), more or less contributed to separating this special station from other stations. Figure 14 shows the clusters of the 20 WIM sites by their geographical locations.

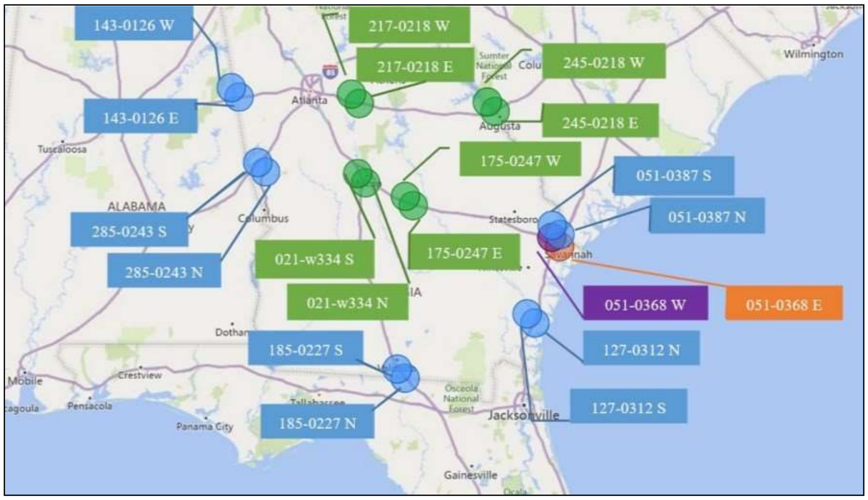

Figure 14. Map. Clusters of WIM sites.

2.9 Pavement Performance Analysis Results

To compare the design implications of the derived clusters with the default TTC groups, the TTC groups that match our clusters were first found based on their similarity by the root mean squared difference in percent, computed by Equation 2.

$$RMSD = \sqrt{\frac{\sum_i^n (y_i - f_i)^2}{n}} \qquad (2)$$

where, n is the total number of vehicle classes (n = 10, including Classes 4 through 13); y_i is the percent occurrence of each truck class based on the clusters; and f_i is the percent occurrence of each truck class based on the default TTC groups. The computed RMSDs are shown in Table 4.

The TTC groups with the minimum RMSDs (the numbers in red in Table 4) to our respective clusters are selected as the best matches. As a result, clusters 0 and 1 are close to TTC group 1; cluster 2 is close to TTC group 4; and cluster 3 is close to TTC group 9. For illustration purposes, the paired clusters and TTC groups are plotted together by the VCD feature in Figure 15.

Table 4. Comparison of Root Mean Squared Differences between the Clusters and the TTC groups.

Group No.	*Cluster 0*	*Cluster 1*	*Cluster 2*	*Cluster 3*
TTC 1	**1.835**	**1.389**	8.7812	17.544
TTC 2	2.359	2.979	5.762	14.500
TTC 3	3.272	3.775	5.541	14.305
TTC 4	6.532	7.1640	**2.536**	10.194
TTC 5	5.701	6.227	3.973	12.181
TTC 6	10.767	11.420	4.106	6.043
TTC 7	10.206	10.764	4.363	7.919
TTC 8	8.931	9.504	3.652	9.459
TTC 9	13.599	14.288	6.441	**4.351**
TTC 10	12.619	13.213	5.932	5.488
TTC 11	13.708	14.342	7.326	7.666
TTC 12	17.714	18.386	10.533	5.867
TTC 13	16.368	16.965	9.701	5.906
TTC 14	23.237	23.861	16.110	7.045
TTC 15	23.455	24.079	16.363	7.434
TTC 16	22.073	22.719	14.899	6.908
TTC 17	20.103	20.721	14.347	14.809

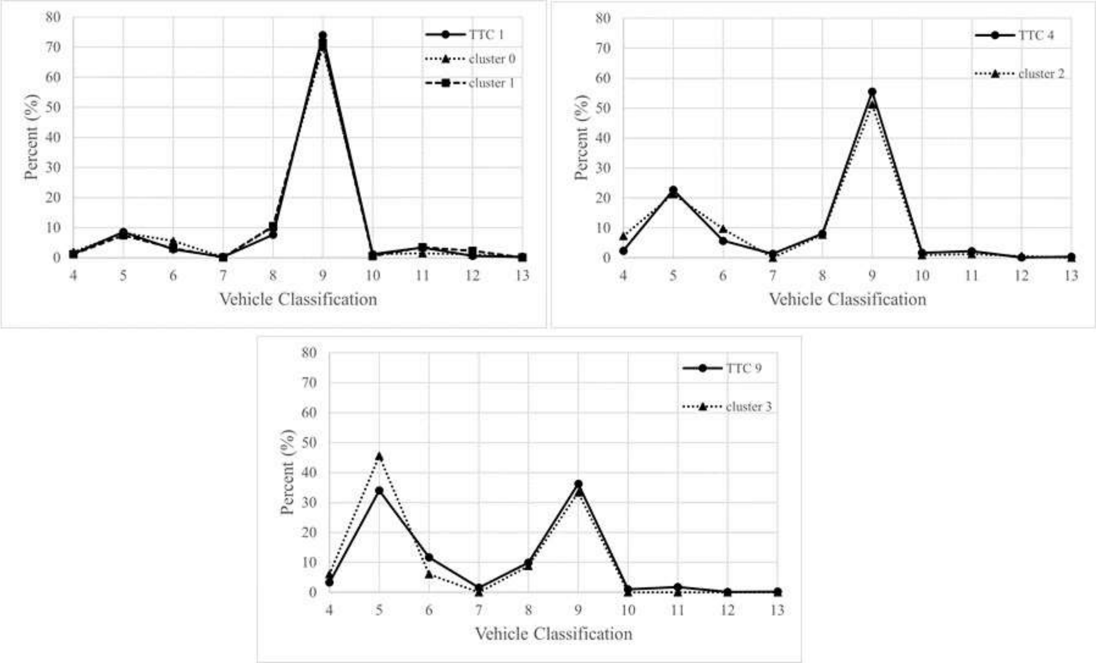

Figure 15. Line graph. Traffic pattern comparison of clusters and default TTC groups.

Both the cluster-based traffic inputs and the corresponding TTC group-based traffic inputs were entered into the AASHTOWare Pavement ME Design software to simulate pavement performance. Two pavement designs (one for jointed plain concrete pavement [JPCP] and one for flexible pavement) were evaluated. The JPCP design consisted of five layers commonly used in Georgia. The top layer was a 12” PCC layer with the recommended JPCP values. The second layer was a 3” AC layer with Superior Performing Asphalt Pavement (Superpave): 64-22. The third layer was a 12” crushed gravel layer, serving as the non-stabilized base. The fourth and fifth layers were two subgrade A-7-6 sections, with a 12” layer on the top and the bottom layer serving as a semi-infinite layer. The flexible pavement design included an 8” asphalt concrete layer followed by a 12” unbound aggregate base layer on A-2-4 subgrade soils.

The AASHTOWare Pavement ME Design software requires a series of traffic inputs, which can be obtained from the WIM data. The software allows pavement design to be conducted with three levels of inputs depending on the data availability. Level 1 uses site-specific data, which provide the highest level of input accuracy for the pavement design. Level 2 uses regional data, which provide an intermediate level of input accuracy for the pavement design. Level 3 uses national or global averages, which provide the least detailed input values. As the purpose of this analysis was focused on the performance comparison of different traffic input scenarios, Level 3 inputs were used. Specifically, the performance difference was analyzed between two traffic input scenarios: one with the cluster-based traffic inputs derived in this project and the other with the national traffic inputs based on the default TTC groups. All the material inputs used in the analysis followed the recently developed input library from The GDOT Pavement ME Design User Input Guide (Kim et al. 2020). The performance curves over a design period of 20 years are plotted in Figure 16 and Figure 17 for JPCP and flexible pavement designs, respectively. For the JPCP, the default TTC groups resulted in worse performance than the cluster group counterparts. The performance gap was the largest between TTC group 1 and clusters 0 and 1 (with about 50 inch in International Roughness Index (IRI) and over 0.1 inch in faulting at the end of the design period). For the flexible pavement, similar performance trends were observed. The TTC groups generally performed equally well or worse than the cluster groups. The apparent gap in bottom-up cracks occurred between TTC group 1 and clusters 0 and 1, which is about 6 percent at the end of the design period. The difference in permanent deformation between TTC group 9 and cluster 3 was about 0.15 inch at the end of the design period. The findings indicate that using the national default TTC groups that closely match the actual traffic data resulted in over-design of the pavement structure, especially for JPCP, in Georgia. This highlights the importance of developing customized TTC groups using state-specific WIM data.

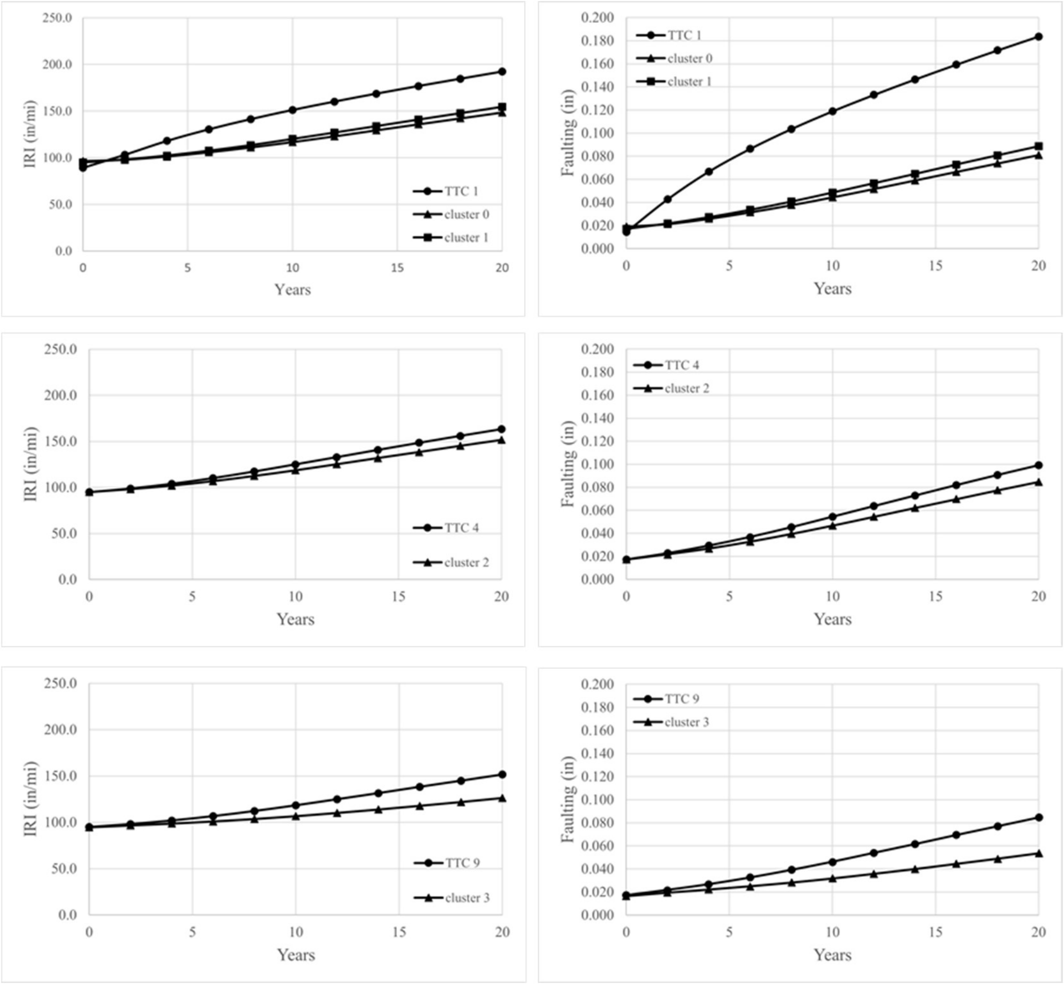

Figure 16. Line graph. JPCP pavement performance comparison of cluster-based traffic inputs and default TTC groups.

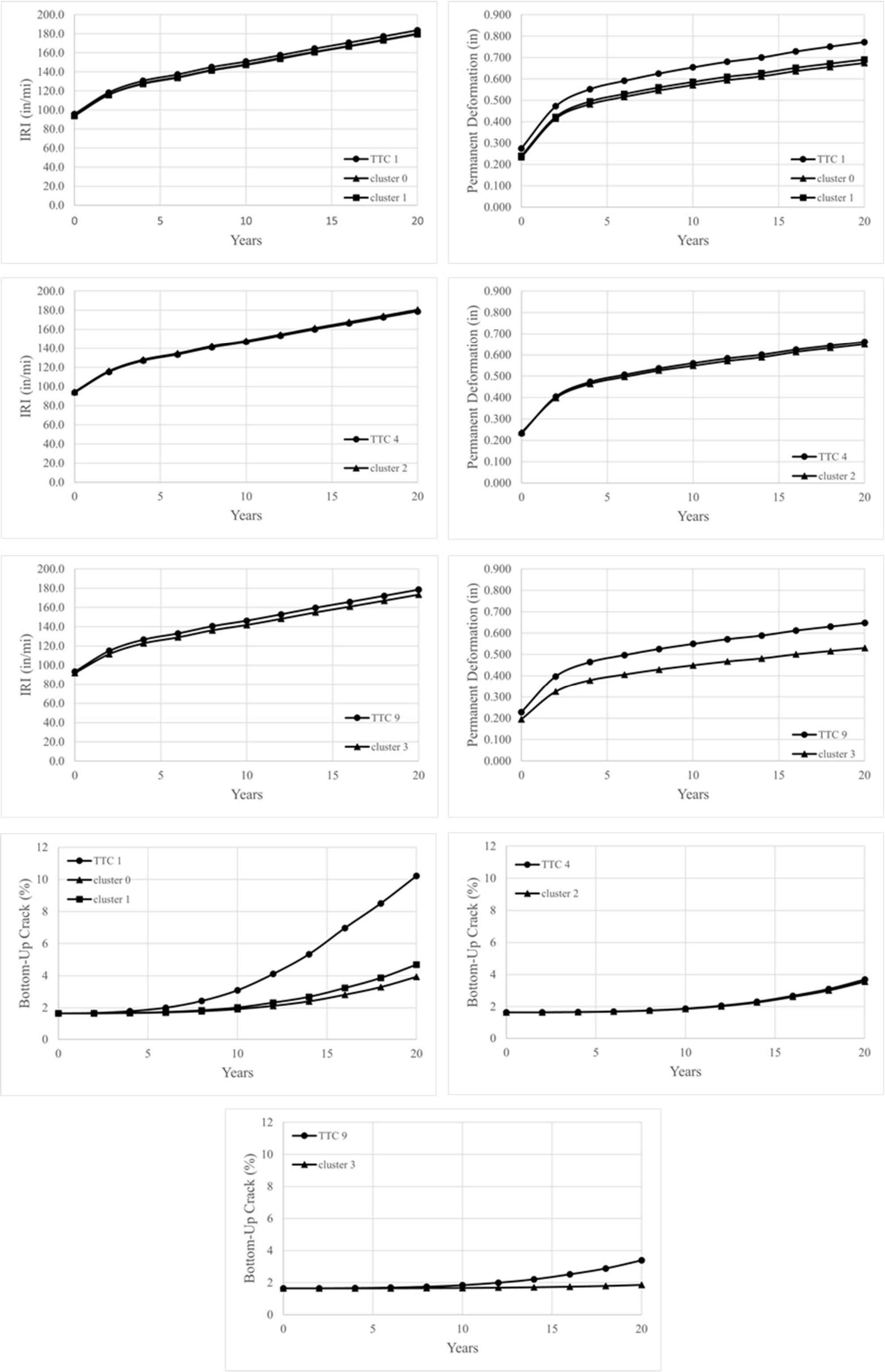

Figure 17. Line graph. Flexible pavement performance comparison of cluster-based traffic inputs and default TTC groups.

CHAPTER 3

3. DEVELOPMENT OF LANE DISTRIBUTION FACTORS FOR GEORGIA USING WIM AND CCS DATA

3.1 Problem Statement

Currently, the Georgia Department of Transportation (GDOT) uses the Lane Distribution Factor (LDF) values that were last updated in 1983. Since then, traffic in Georgia has changed dramatically, especially over the recent decade, due to considerable growth in the state's economy and population, as well as demographic changes. Since the currently adopted LDFs are outdated and may not reflect actual truck traffic lane distributions, a study based on the latest lane-specific vehicle counts and classification data is needed to verify and update, if necessary, the LDF values in support of GDOT's pavement design practice.

3.2 Lane Distribution Factor

LDF is simply defined as the percentage of truck volumes traveling in the outermost lane, referred to as the design lane, to the total truck volumes of all lanes in one travel direction (Lu & Harvey 2006). LDF is one of the critical pavement design parameters, which determines the amount of 18-kip ESAL (Equivalent Single Axle Load) in the design lane. Equation 1 is typically used to estimate the design ESAL. Considering the multiplicative effect of LDF on the design ESAL, it is important to ensure the accuracy of LDF to avoid potential over- or under-design of pavement.

$$\mathrm{ESAL_{Design}} = \left(\frac{\mathrm{ADT_1} + \mathrm{ADT_N}}{2}\right) \times \sum_{\mathrm{i}} (\mathrm{P_i} \times \mathrm{LEF_i}) \times 365 \times \mathrm{N} \times \mathrm{DDF} \times \mathrm{LDF} \qquad (1)$$

where,

P_i = percent of vehicles in each of the three categories: (1) passenger cars & pickup trucks, (2) single unit trucks, and (3) combination trucks.

LEF_i = load equivalency factor for each of the three vehicle categories above.

N = design period in years (e.g., 20 years)

DDF = directional distribution factor

LDF = lane distribution factor

Generally, LDF varies by area/ facility type, the number of lanes, and traffic volume. For two-lane highways, (one lane in each direction), the LDF is 1.0, where drivers have no choice, but use the only lane available. For facilities of more than one lane in each direction, LDF varies by other factors, such as AADT, geometric, and site-specific conditions (Haider et al. 2018). Typically, LDF decreases with the increase in the number of lanes as more lane options are available to drivers. Based on the field observations, the outermost lane usually carries the highest percentage of truck traffic, referred to as the design lane for the purpose of pavement design.

The LDF values currently adopted in the Pavement Design Manual (GDOT, 2019) are shown in Tables 5 and 6. Table 5 shows the recommended range of LDF values by area/ facility types. Table 6 shows LDF values for multilane highways with respect to specific ADT levels and the number of lanes. As mentioned previously, the last update for Table 5 was in December 2005 and Table 6 LDF values were based on a previous study conducted in 1982-1983.

Table 5. Lane distribution factors by facility type (GDOT Pavement Design Manual 2019).

Facility	LDF (in percent)
Four lane Rural Freeway	85-100
Four Lane Urban Freeway	60-80
Six Lane Rural Freeway	70
Six Lane Urban Freeway	60
Six Lane Rural Highway Free Access	70-100
Six Lane Urban Highway -Free Access	60-80
Two Lane Highway and Ramps	100

Table 6. Lane distribution factors for multilane highways (GDOT Pavement Design Manual 2019)

One Way ADT	2 Lanes (one Direction)		3+ Lanes (one-Direction)		
	Inner	Outer	Inner*	Center	Outer
2,000	6**	94	6	12	82
4,000	12	88	6	18	76
6,000	15	85	7	21	72
8,000	18	82	7	23	70
10,000	19	81	7	25	68
15,000	23	77	7	28	65
20,000	25	75	7	30	63
25,000	27	73	7	32	61
30,000	28	72	8	33	59
35,000	30	70	8	34	58
40,000	31	69	8	35	57
50,000	33	67	8	37	55
60,000	34	66	8	39	53
70,000	--	--	8	40	52
80,000	--	--	8	41	51
100,000	--	--	9	42	49

* Combined inner one or more lanes.

** Percent of all trucks in one direction (note that the proportion of trucks in one direction sums to 100 percent).

The literature review reveals limited research on estimating lane distribution factors. The most relevant studies are discussed in the following section.

3.3 Literature Review

Albright and Blewett (1988) conducted a study in which a model was developed to estimate LDF values on tangent sections of the New Mexico rural interstates. Based on the study, the total vehicle volume and truck percentage are statistically significant in terms of truck lane use and should be considered as explanatory variables. Also, LDF has been proved to be a function of flow rate (Chatterjee et al., 2016). Based on this study, the increase in flow rate would equalize the LDF value. Kumar and Reddy (2014) conducted a case study in which the LDFs for two-lane, four-lane, and undivided highways were evaluated against the suggested values for two sections of National Highways (NH7 and NH9) in India. The results proved that there are anomalies between the obtained LDF values and the LDF values suggested by the IRC pavement design procedure. Thus, fixation of the Lane Distribution Factor for these sections is recommended. Another study (Fwa and Li, 1995) was conducted in Singapore to evaluate the effects of certain factors on the lane distribution of trucks. These factors include the functional class of roads, the number of travel lanes, the total directional traffic volume, and the volume of truck traffic. Statistical regression models were developed to estimate truck volume in the critical lane. The study indicated that changes in land-use development, economic, and social structures are effective on travel characteristics, traffic flow composition, and hence lane distribution factors.

Thus, highway agencies must develop regression models and update them periodically to reflect such changes and provide more accurate LDF for pavement design.

Besides the regression approach, machine learning approach (e.g., clustering) was attempted as well. Lu and Harvey (2006) utilized WIM data to characterize truck traffic to assist with mechanistic–empirical pavement design in California. Kernel density estimation was performed to estimate the density function of LDF for highways with different numbers of lanes. The analysis showed that when there are two lanes in one travel direction, more than 90% of the truck traffic will use the outside lane, and when there are three or more lanes in one travel direction, more than 90% of the truck traffic will use the outermost two lanes.

3.4 Traffic Data Collection

The GDOT's Office of Transportation Data (OTD) has a comprehensive traffic count program. Traffic data is collected by permanent Continuous Count Station (CCS) sites, portable count stations, permanent and continuous Weigh-In-Motion (WIM) sites, and temporary WIM sites (Wiegand 2018).

3.4.1 WIM Sites

The WIM sensors embedded in the pavement have the potential to collect continuous high-resolution traffic data, such as vehicle counts, gross vehicle weight, axle configuration, axle weight data, and speed (Kim et al., 2021). WIM data are utilized for various purposes, such as the design of pavements or bridges, highway and traffic planning, legislative/ regulatory studies, capacity studies, enforcement, and inspection purposes (FHWA 2018 & Wiegand 2018). Although there are several types of WIM systems, WIM technology generally consists of several main components. Sensors embedded in the roadway surface or under a bridge deck detect axles and weights and classify the passing vehicles. Electronics control the system function to process sensor outputs. Support devices power the WIM electronics to dispatch the collected data to a remote server. Finally, software installed in the WIM electronics process the measurements, analyze the format, and store the collected data (FHWA 2018).

3.4.2 CCS Sites

Since July 2017, OTD in GDOT has had hundreds of CCS sites installed on roadway systems throughout the state. These sites operate 24 hours per day, seven days per week, 365 days per year, excluding the necessary maintenance periods. The collected data from CCS sites are vehicle classification and traffic volume data (Wiegand 2018).

In this study, the lane-specific vehicle counts and classification data for the most recent four years (2018-2021) were obtained from all active CCS sites in Georgia. The WIM data from 29 active WIM sites in 2021, collected as part of another study (Chorzepa et al., 2022), was also utilized. The locations of these CCS and WIM sites are depicted in Figure 18, where blue circles denote the CCS and red circles denote the WIM sites.

3.5 Data Analysis

The raw CCS and WIM data are processed to compute LDFs together with other features, including directional AADT, the number of lanes, truck volumes and percentages, area, and facility types. Vehicle classes 5 through 13 (according to the FHWA classification system) are considered as trucks. Given the definition of the LDF, yearly traffic data are first compiled for each lane in each travel direction, resulting in AADT and AADTT by lane and by direction. Then, the corresponding LDF values are computed for each direction. For each of 2-lane (one travel direction) facilities, two LDF values are computed, one for the inner lane (denoted as LDF_inner) and one for the outer lane (denoted as LDF_outer). For each of facilities with three or more lanes (one travel direction), three LDF values are computed, including one for the outermost lane (LDF_outer), one for the second outmost lane (denoted as LDF_center), and one for the remaining lane(s) (denoted as LDF_inner). Besides the LDF values, explanatory variables (features) are compiled from the CCS and WIM data as well and are summarized in Table 7. It should be noted that regrouping of the original functional classes of facilities into two categories (i.e., Interstate and Others) was based on statistical analysis of the data.

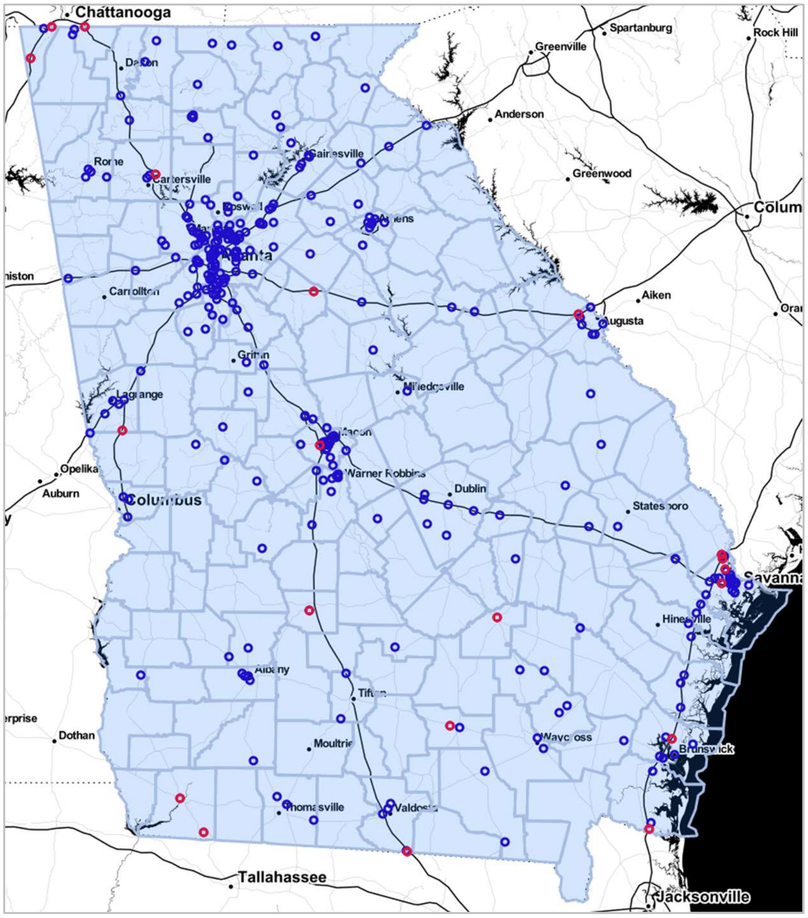

Figure 18. Map. Locations of active CCS and WIM sites in Georgia.

Table 7. Description of variables

Variable	Description	Statistics of Dataset
AADT	Annual Average Daily Traffic	Mean: 29,354 Min: 1,207 Max: 161,449
lnAADT	Natural logarithm of AADT	Mean: 9.772 Min: 7.096 Max: 11.992
Urban	Dummy variable to indicate whether the facility is in an urban or rural setting.	1 – Urban (count: 997) 0 – Rural (count: 303)
Interstate	Dummy variable to indicate whether the facility is Interstate, other Freeways or Expressways.	1 – Interstate (count: 747) * 0 – Others (count: 553)
3+ln	Dummy variable to indicate if the facility has 3 or more lanes (one travel direction).	1 – 3 or more lanes (count: 483) 0 – 2 lanes (count: 817)
Lanes	Number of lanes (one travel direction)	Min: 2, Max: 7, Mean: 2.76
Truck percentage	Percent of trucks in the traffic (one travel direction)	Mean: 12.02% Min: 0.71%, Max: 61.32%

* Includes other Freeways and Expressways.

Additionally, to evaluate the potential effect of the COVID-19 on statewide traffic characteristics, the statewide mean AADT, AADTT were computed and are presented in Figure 19. Similarly, the statewide mean LDF values were computed and are presented in Figure 20. As seen in Figure 19, a significant traffic drop is observed in 2020 due to the COVID-19. Although statewide traffic increases slightly in 2021, it is still lower than the pre-COVID-19 condition. Nevertheless, the statewide truck traffic increases steadily throughout the COVID-19. As shown in Figure 20, the LDF values remain relatively constant before and after the COVID-19.

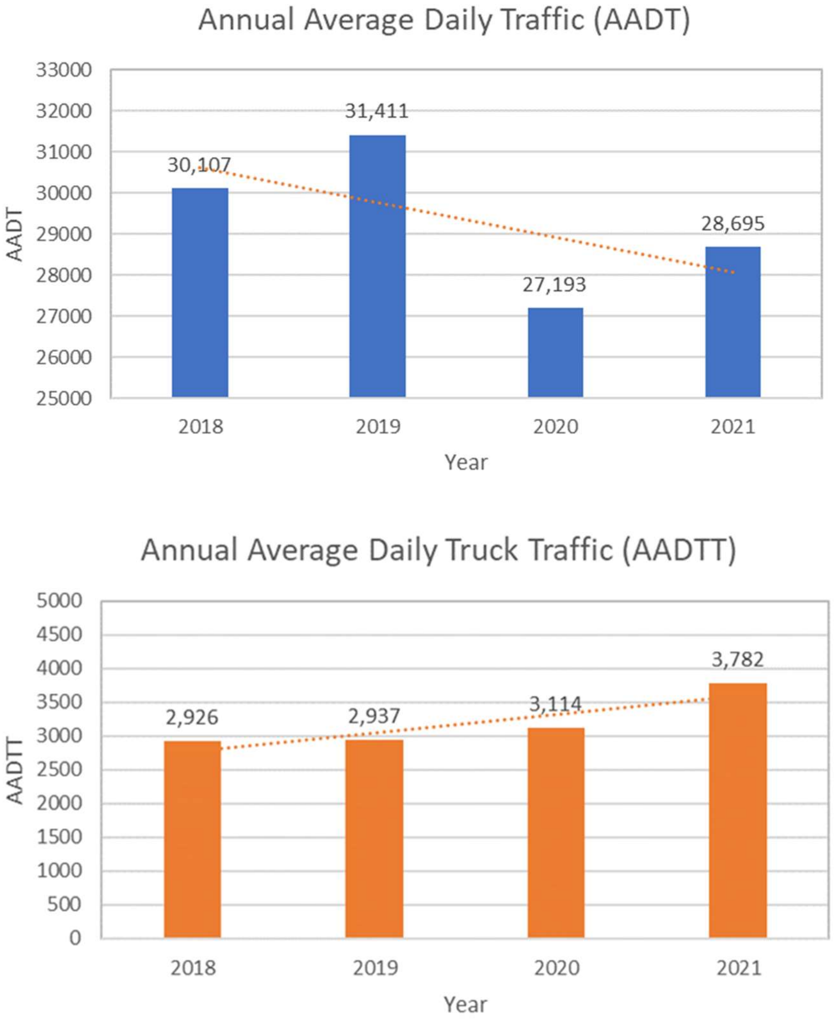

Figure 19. Bar chart. Statewide traffic by year.

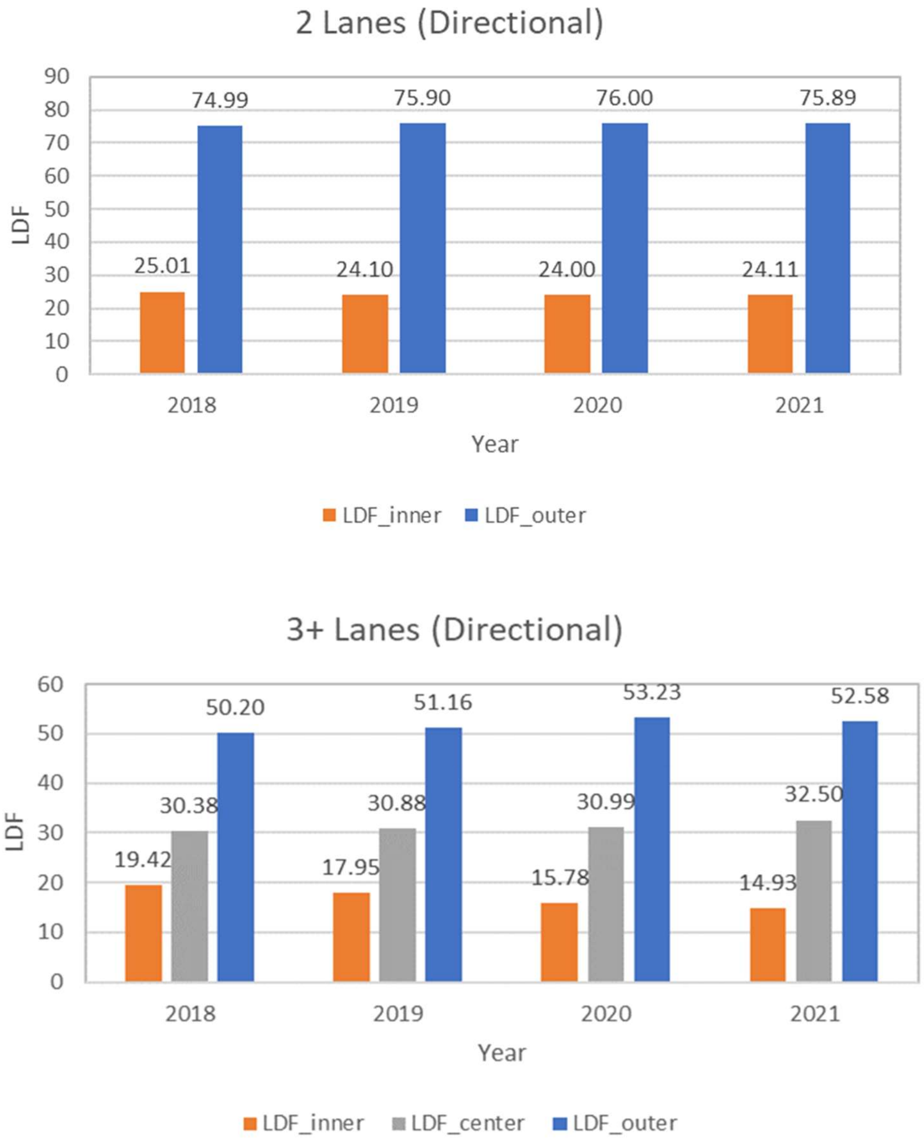

Figure 20. Bar chart. Statewide LDFs by year.

3.6 Estimating Lane Distribution Factor

Logistic regression is one of the most popular statistical approaches which models the probability of a discrete outcome given one or more explanatory variables (Edgar & Manz, 2017). Since LDF is defined as the percentage of directional truck traffic traveling in the outermost lane (the lane with the highest percentage of truck volume, referred to as the design lane), it is natural to model LDFs as probability distribution across lanes. To capture the effect of the number of lanes (one travel direction), a hierarchical modeling framework is adopted with a higher-level logistic model (referred to as Model A) to estimate LDF_outer (i.e., LDF for the outermost lane) and a lower-level logistic model (referred to as Model B) to estimate LDF_center (i.e., LDF for the second outmost lane) for facilities with three or more lanes in one travel direction. In this study, Model B is specified such to estimate the "relative" LDF for the second outermost lane by disregarding the outmost lane. Model A is fit by considering all relevant features. Our analysis indicates that grouping the number of lanes into two categories (i.e., 2 lanes and 3+ lanes) does improve model fitting as compared to using the number of lanes directly as ordinal features, which substantiates the original design of the LDF table in the GDOT's pavement design manual. On the other hand, by closely examining the LDF values with respect to AADTs in the currently adopted design table, it becomes apparent that LDF is logarithmically related to AADT. Based on our data analysis, the logarithm transformation of AADT dramatically improves model fitting, thus was adopted. Additionally, the COVID-19 was also considered as a feature by coding it as a dummy variable. It turns out that the effect of the COVID-19 on LDF is not significant, which concurs with the stable LDF values before and after the COVID-19 in Figure 20.

Similar to Model A, Model B is fit only for facilities with 3+ lanes by simply disregarding the outermost lane and treating the second outermost lane as the "outmost lane". The model estimation results are summarized in Table 8 and Table 9 for Model A and Model B, respectively.

Table 8. Model A - Estimating LDFs for the outermost lane (LDF_outer)

Variable	Coef	Std Err	t statistic	p value	95% CI	
Const	5.453	0.207	26.391	0.000	5.048	5.858
LnAADT	-0.468	0.024	-19.515	0.000	-0.515	-0.421
Urban	-0.311	0.035	-8.797	0.000	-0.381	-0.242
Interstate	0.837	0.038	21.860	0.000	0.762	0.913
3+ln	-0.822	0.043	-19.315	0.000	-0.905	-0.738
F statistic:	679.20	p value:	0.000			
R-squared:	0.676					
No. of obs:	1,300					

Table 9. Model B - Estimating LDFs for the second outermost lane (LDF_center)

Variable	Coef	Std Err	t statistic	p value	95% CI	
Const	16.854	0.653	25.791	0.000	15.570	18.138
LnAADT	-1.566	0.069	-22.809	0.000	-1.701	-1.431
Urban	-0.438	0.141	-3.093	0.002	-0.716	-0.160
Interstate	1.636	0.172	9.486	0.000	1.297	1.974
F statistic:	222.30	p value:	0.000			
R-squared:	0.582					
No. of obs:	483					

As shown in Table 8, increase of LnAADT will decrease LDF_outer as indicated by the negative coefficient for lnAADT. Facilities in urban areas have a lower LDF_outer as compared to those in rural areas. Interstates and other Freeways/ Expressways have a higher LDF_outer than the facilities of lower functional classes. The negative sign of "3+ln" reveals that facilities with three or more lanes (one travel direction) have a lower LDF_outer than facilities with two lanes (one travel direction). Similar feature effects are observed for Model B (see Table 9). The F statistics (lower p-values) indicate good overall fitting of both Model A and Model B with R-squared of 0.676 and 0.582, respectively.

Since Model A and Model B consider area/ facility types, the resulting LDF values are not directly comparable to the LDF values currently adopted in the GDOT pavement design manual. For comparing purposes, Model A and Model B are refit by removing the area/ facility types as features, referred to as Simplified Model A and Simplified Model B. The estimation results of the simplified models are summarized in Table 10 and Table 11, respectively.

Table 10. Simplified model A

Variable	Coef	Std Err	t statistic	p value	95% CI	
Const	3.849	0.229	16.831	0.000	3.400	4.297
LnAADT	-0.284	0.025	-11.422	0.000	-0.332	-0.235
3+ln	-0.710	0.053	-13.439	0.000	-0.814	-0.607
F statistic:	636.70	p value:	0.000			
R-squared:	0.495					
No. of obs:	1,300					

Table 11. Simplified model B

Variable	Coef	Std Err	t statistic	p value	95% CI	
Const	15.910	0.708	22.478	0.000	14.520	17.301
LnAADT	-1.374	0.066	-20.970	0.000	-1.502	-1.245
F statistic:	439.80	p value:	0.000			
R-squared:	0.478					
No. of obs:	483					

It should be noted that although the truck volume is an influential factor considered in the previous studies (e.g., Albright and Blewett, 1988 and Fwa and Li, 1995), our analysis indicates that truck percentage is not significant conditional upon AADT and area/ facility type. However, the effect of truck volume should be continuously monitored for future consideration.

3.7 Results

For implementation of the study results, LDF values are updated by applying the developed models. First, the simplified models are applied to estimate LDF values and compare with the LDF values currently adopted in the GDOT pavement design manual. The updated LDF design table based on the simplified models is shown in Table 12. Compared with the currently adopted LDF values (Table 6), the new LDF values are generally lower for 3+lane facilities and 2-lane facilities with low AADT.

Table 12. Updated lane distribution factors for multilane highways

One Way ADT	2 Lanes (one Direction)		3+ Lanes (one Direction)		
	Inner	Outer	Inner*	Center	Outer
2,000	16	84	0	27	73
4,000	18	82	0	31	69
6,000	20	80	1	33	66
8,000	21	79	1	35	64
10,000	22	78	1	36	63
15,000	25	75	3	37	60
20,000	26	74	4	38	58
25,000	27	73	5	38	57
30,000	28	72	7	38	55
35,000	29	71	8	38	54
40,000	30	70	10	37	53
50,000	31	69	13	36	52
60,000	33	67	15	34	50
70,000	-	-	18	33	49
80,000	-	-	21	31	48
100,000	-	-	25	28	47

* Combined inner one or more lanes

Knowing that area/ facility types are significant features underlying the variation of LDFs, separate design LDF tables (Tables 13-16) are also developed based on Model A and Model B with respect to different area/ facility types.

Table 13. Updated lane distribution factors for multilane highways (Urban Interstate/Freeways/Expressways)

One Way ADT	2 Lanes (one Direction)		3+ Lanes (one Direction)		
	Inner	Outer	Inner*	Center	Outer
2,000	8	92	0	17	83
4,000	11	89	0	22	78
6,000	13	87	0	25	75
8,000	15	85	1	27	72
10,000	16	84	1	29	70
15,000	19	81	2	33	66
20,000	21	79	3	35	63
25,000	22	78	4	36	60
30,000	24	76	5	36	58
35,000	25	75	7	37	56
40,000	27	73	9	37	55
50,000	29	71	12	36	52
60,000	30	70	15	35	50
70,000	-	-	19	33	48
80,000	-	-	22	32	47
100,000	-	-	28	28	44

* Combined inner one or more lanes

Table 2. Updated lane distribution factors for multilane highways (Rural Interstate/Freeways/Expressways)

One Way ADT	2 Lanes (one Direction)		3+ Lanes (one Direction)		
	Inner	Outer	Inner*	Center	Outer
2,000	6	94	0	13	87
4,000	8	92	0	17	83
6,000	10	90	0	20	80
8,000	11	89	0	22	78
10,000	12	88	0	24	76
15,000	14	86	1	27	72
20,000	16	84	1	29	70
25,000	18	82	2	30	67
30,000	19	81	3	31	65
35,000	20	80	4	32	64
40,000	21	79	5	33	62
50,000	23	77	7	33	60
60,000	24	76	9	33	58
70,000	-	-	12	32	56
80,000	-	-	14	31	55
100,000	-	-	19	29	52

* Combined inner one or more lanes

Double underlined: extrapolated values, use with caution.

Table 15. Updated lane distribution factors for multilane highways (Urban Others)

One Way ADT	2 Lanes (one Direction)		3+ Lanes (one Direction)		
	Inner	Outer	Inner*	Center	Outer
2,000	17	83	0	32	68
4,000	22	78	1	38	61
6,000	26	74	3	41	56
8,000	28	72	4	43	53
10,000	30	70	6	44	50
15,000	35	65	11	43	45
20,000	38	62	17	41	42
25,000	40	60	22	38	40
30,000	42	58	27	35	38
35,000	44	56	32	33	36
40,000	46	54	-	-	-
50,000	-	-	-	-	-
60,000	-	-	-	-	-
70,000	-	-	-	-	-
80,000	-	-	-	-	-
100,000	-	-	-	-	-

* Combined inner one or more lanes

Double underlined: extrapolated values, use with caution.

Table 163. Updated lane distribution factors for multilane highways (Rural Others)

One Way ADT	2 Lanes (one Direction)		3+ Lanes (one Direction)		
	Inner	Outer	Inner*	Center	Outer
2,000	13	87	0	25	74
4,000	17	83	1	31	68
6,000	20	80	1	35	64
8,000	22	78	2	37	60
10,000	24	76	3	39	58
15,000	28	72	7	40	53
20,000	31	69	10	40	50
25,000	33	67	14	39	47
30,000	35	65	18	37	45
35,000	37	63	22	35	43
40,000	38	62	-	-	-
50,000	-	-	-	-	-
60,000	-	-	-	-	-
70,000	-	-	-	-	-
80,000	-	-	-	-	-
100,000	-	-	-	-	-

* Combined inner one or more lanes

Double underlined: extrapolated values, use with caution.

The distinct LDF values across area/ facility types suggest that separate LDF tables should be adopted for different area/ facility types. By comparing Tables 13-16 with Table 6, the use of the current design LDF values would generally lead to under-design of Rural Interstate/Freeways/Expressways and over-design of other facilities. To facilitate the design practice, a web application is developed to display the computed LDF values per user's design inputs.

3.8 Conclusion

In this study, the latest lane-specific vehicle count, and classification data are obtained from all active CCS stations and WIM sites throughout the state of Georgia. LDF values are computed for each CCS and WIM site and correlated with relevant features, including AADT, area type, facility type, the number of lanes, truck percentage, as well as considering the effect of the COVID-19. A hierarchical modeling framework is developed, consisting of two logistic models: (1) a higher-level model for estimating LDF for the outmost lane (LDF_outer) for all facilities, and (2) a lower-level model for estimating LDF for the second outmost lane (LDF_center) for facilities with 3 or more lanes (one travel direction). The feature analysis reveals that grouping the number of lanes into two categories (i.e., 2 lanes and 3+ lanes) improves model fitting than treating the actual number of lanes as an ordinal feature. Following similar analysis, the facility types are regrouped into two categories: Interstate (including other Freeways and Expressways) and others. The existing area types (Urban versus Rural) are retained. Consistent with current practice, logarithm transformation of AADT is applied, resulting in improved model fitting. The effect of the COVID-19 on LDF is found to be insignificant.

Based on the study, it is highly recommended that separate LDF tables (Tables 13-16) are adopted for pavement design in light of the significant roles that the area and facility types play in determining LDF values. Given the anticipated economic growth and evolving socioeconomic characteristics of the state of Georgia as well as continuous adoption of new or emerging technologies (e.g., E-mobility, statewide deployment of charging stations, semi-autonomous or autonomous truck platooning, emerging connected and autonomous vehicles, etc.), regularly updating the LDF values (e.g., every 3 years) is recommended to capture the changes in traffic characteristics over time.

CHAPTER 4

4. REMOTE SENSING TECHNIQUES FOR PAVEMENT MAINTENANCE SCHEDULING PURPOSES

4.1 Remote Sensing Methodologies in Pavement Assessment

Remote sensing is the technology to capture data from the earth's surface through electromagnetic radiation and the science to analyze these data and the geo-bio-physical properties to understand the various geographical phenomena on our planet (Navalgund et al., 2007). Unlike other sensing technologies, remote sensing promised to be a cost-effective approach where the data are collected from all around the globe regularly (Goezt et al., 1983).

Pavement deterioration is the combined result of either traffic loads or environmental factors during the pavement's service life (Adlinge and Gupta, 2013). Asphalt pavements lose their first-day quality and deteriorate gradually over time. Surface and fatigue cracking, potholes, rutting, and swelling are the most common asphalt pavements deterioration by which the flexible pavement surface can lose its specific properties such as smoothness, skid-resistance, and macro-texture (Schnebele et al., 2015). Figure 21 illustrates the aging process of a typical asphalt pavement surface over time. During the first years of the service life, the pavement loses a vast amount of bitumen due to volatilization, absorption, oxidation, and photochemical reaction with solar radiation, causing the pavement to be less viscous, brittle, and vulnerable (Herold, 2014 and Pan et al., 2017 and Andreou, 2011) (Figure 21(b)). Figure 21(c) shows the moderately aged pavement in which the stone content is exposed. Figure 21(d) demonstrates a heavily aged pavement in which the weathering variables intensify the deterioration process. Finally, structural deformations occur in the form of cracks, rutting, and potholes, as seen in Figure 21(e) (Pan et al., 2017).

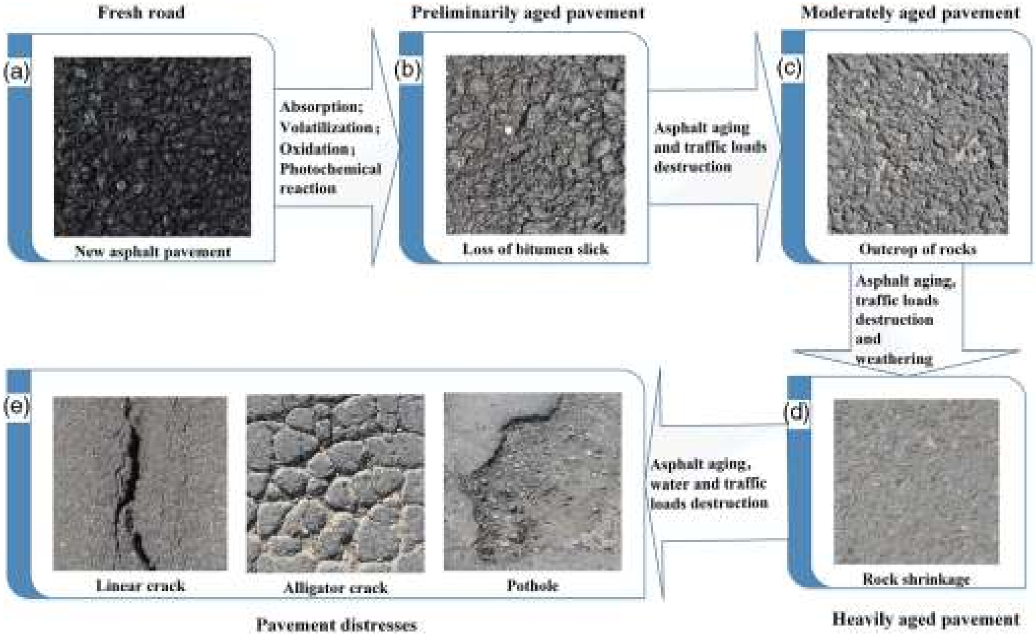

Figure 21. Aging process of asphalt pavement over time [Pan et al., 2017].

In terms of the remote sensing, the newly paved asphalt exhibits absorption features due to the presence of oily components. When the pavement surface deteriorates by either aging process or by factors like photochemical reaction or influence of heat, the oily components in the asphalt mix decrease which causes the reduction of absorption and increase of reflectance in all parts of the wavelength spectrum (Herold, 2004). Figure 22 shows the spectral characteristics of three asphalt pavement sections with different aging levels measured by Analytical Spectral Devices (ASD) (Herold, 2004). However, all three samples are free of any obvious structural damages or cracks. The pavement condition index (PCI) and the structural index (SI) are also shown with image

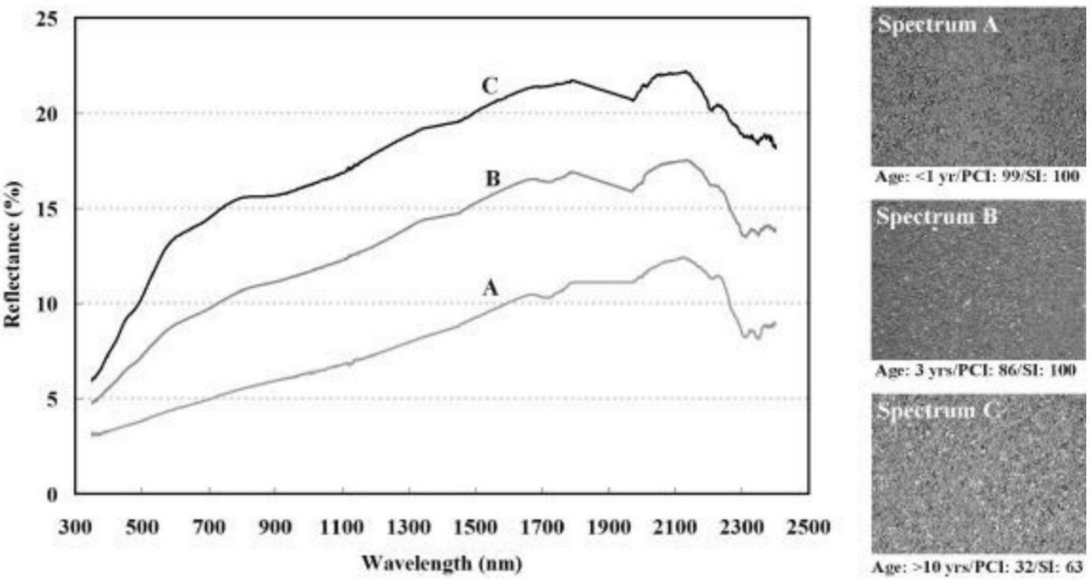

Age: <1 yr/PCI: 99/SI: 100

Age: 3 yrs/PCI: 86/SI: 100

Age: >10 yrs/PCI: 32/SI: 63

Figure 22. Line graph. Spectral variation of asphalt pavement by aging (Herold, 2004).

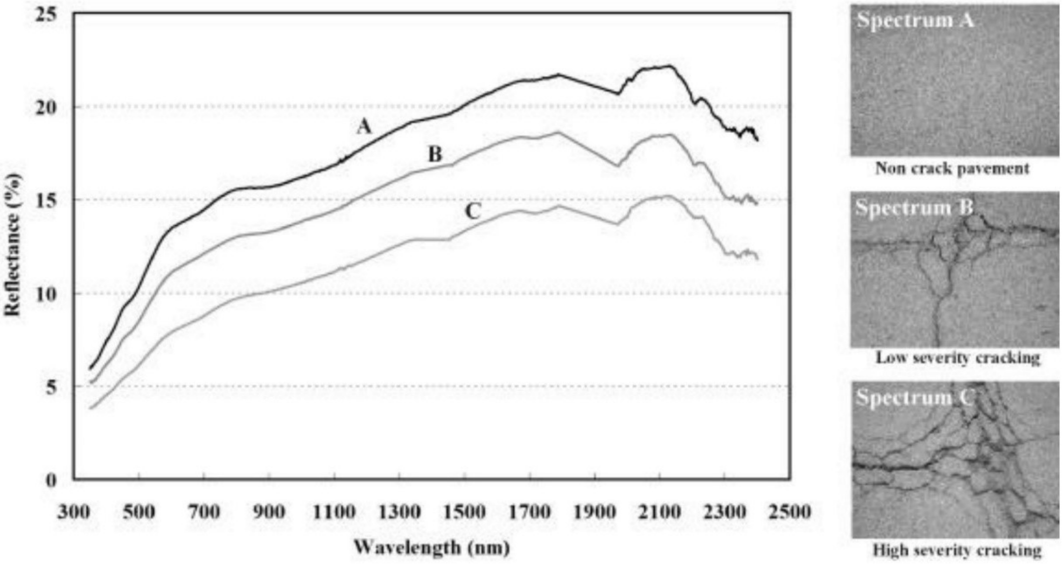

Non crack pavement

Low severity cracking

High severity cracking

Figure 23. Line graph. Spectral variation of asphalt pavement by structural damages (Herold, 2004).

examples of the pavements. Spectrum A reflects a newly paved road with strong absorption features due to the presence of oily components. The overall reflection is very low, with the minimum reflectance near 350 nm and a linear rise towards longer wavelengths. Spectrums B and C represent intermediate and old/ deteriorated asphalt pavement sections, respectively. The erosion and aging of the asphalt mix cause the road surface to be less viscous and more vulnerable to structural damages and cracks. Figure 23 also shows the spectral measurements of asphalt pavement sections with different severity levels of structural damage and cracks. The general surface reflectance spectra are similar to the spectra in Figure 22. However, cracks impact the brightness in all parts of the spectrum. Cracks and structural damages cause shadows and make reflectance differences of up to 7-8% between healthy pavement and severely cracked pavements. When cracking occurs, deeper layers with higher contents of the asphalt mix are exposed to the air. Increased hydrocarbon absorption features thus reduce the reflectance. This phenomenon proves one of the limitations in monitoring road conditions using hyperspectral remote sensing.

The objective of this study is to leverage the satellite images for infrastructure health monitoring based on the historical datasets from the satellite imagery. In this approach, the surface reflectance is extracted from the pavement sections of the Georgia state roads. Moreover, the international roughness index (IRI) measurements throughout Georgia state are provided to correlate the IRI values and the corresponding spectral characteristics of different pavement sections using historical datasets and statistical analysis methods. The goal is to use freely available satellite imagery to indicate the distress severity of different pavement sections and schedule maintenance on time without needing an on-site distress survey.

In the following section, recent approaches used for the application of remote sensing in monitoring road conditions are presented.

4.2 Literature Review

Road quality mapping with in-situ measurements is expensive and time-consuming. To overcome the issue, Karimzadeh and Matsuoka (2021) measured the in-situ international roughness index (IRI) using a Quarter Car (QC). They then developed new equations for constructing a road quality proxy map (RQPM). Intermediate resolution Sentinel-2 images are utilized in this study. Discriminant analysis methods such as optimum index factor (OIF) and norm R provide a tool for generating proxy maps and mitigating hazards at the network level pavement management systems. Recently a study has investigated the impact of the COVID-19 pandemic on urban road traffic volume using video remote sensing (Macioszek and Kurek, 2021). The study obtains data from Traffic Control Center (TCC), analyses the road traffic volume before and during the restrictions, and attempts to predict the traffic patterns at specific stages of the pandemic. Several studies have employed multispectral and hyperspectral data to map the road network, but few attempts were made to map the road surface conditions (Andreou, 2011). Tosti et al. (2021) investigated integrating information from satellite remote sensing and ground-based non-destructive testing (NDT) methodologies for transport infrastructure monitoring purposes. The research revealed that the stand-alone application of these techniques is constrained due to multiple factors such as data resolutions and land coverage limitations. Herold et al. (2004) investigated the optimal wavelengths for mapping urban materials using Airborne Visible/ Infrared Imaging Spectrometer (AVIRIS) data. The maximum likelihood classifier generates the map, separating roads of different materials, such as asphalt, concrete, and gravel. The map also differentiates the surface materials in terms of age and condition. However, the developed map is restricted by a spatial sensor resolution of 4.0 m. Detecting the damage to forest roads wearing course is another research completed using different methods of remote sensing in the Czech Republic (Hrůza et al., 2018). The study aims to verify the possibility and accuracy of damaged bituminous forest roads detected by various remote sensing methods: close-range photogrammetry, terrestrial laser scanning, mobile laser scanning, and airborne laser scanning. The results indicated that close-range photogrammetry and terrestrial laser scanning methods have the highest accuracy and are sufficient for monitoring the asphalt-wearing course of forest roads. Andreou et al. (2011) investigated the application of hyperspectral remote sensing for mapping asphalt road conditions. Filed hyperspectral data obtained from GER1500 radiometer utilized to provide spectral measurements for developing a spectral library for asphalt. Spectral features analysis indicated that pavement condition is affected by asphalt age, material quality, and road circulation. Based on the results, the following machine learning-based analysis methods are the most appropriate for detecting asphalt pavement conditions: Principal Component Analysis (PCA), thresholding of color transformation images, unsupervised classification, Iterative Self-organizing Data Analysis (IsoData), supervised classification Spectral Angle Mapper (SAM), and texture measurements using Grey-level Co-occurrence Matrix operator. A study was conducted to observe defective roads utilizing the multispectral imageries of a flying drone called Parrot Sequoia (Mukti & Taher, 2021). Potholes in the images were then recognized using techniques such as band combination and supervised classification. The results showed that the low resolution of the imageries potentially limits the pothole detection objective.

4.3 Remote Sensing Platforms

Remote sensing is a technology in which the object/area of interest is either very close (1 cm) to or very far (more than 1 million m) from the sensor (Jensen, 2009) and can be implemented through various platforms, including moving vehicles, airplanes, Unmanned Aerial Vehicles (UAVs), and satellites. These techniques offer non-destructive and temporally systematic evaluation methods compared to traditional procedures such as coring and field surveys. In the following, a brief description of common platforms is discussed.

4.3.1 Airplane

Aerial platforms provide higher spatial resolution images and much more tasking flexibility compared with other platforms. For instance, airplanes can carry various sensors and devices gathering imagery data from altitudes ranging from 300 to 13,000 m (Job, 2021) while other platforms cannot maneuver by changing their altitude. Most DOTs make extensive use of aerial photography in accordance with highway planning and mapping applications. Required data could be collected from suborbital platforms like airplanes and helicopters when the weather condition is appropriate (Jensen, 2009).

4.3.2 Unmanned Aerial Vehicle (UAV)

UAV is an aircraft with neither a human pilot nor a passenger, which has been widely used in transportation engineering in recent years. UAVs are very cost-effective in providing "bird’s eye view" images for a variety of smart transportation applications (Coifman et al., 2004). UAVs can provide high resolution and near real-time imagery, less expensive than air-borne and space-borne platforms (Job, 2021). However, ego-motion issue caused by either pilot or wind is considered the most significant technical challenge in automatic UAVs (Ke et al., 2018). Garilli et al. (2021) developed two supervised classification approaches (a semi-automatic classification plugin for

QGIS and a convolutional neural network) using UAV photogrammetry to detect stone pavement's pattern.

4.3.3 Vehicle

Survey vehicles are another type of sensing platforms in which data are collected using laser scanners, photo/video or thermal cameras, and Ground Penetrating Radar (GPR). GPR, Ultrasonic Testing (UT), and Acoustic Emission (AE) are mostly used for subsurface defects detecting (Golrokh et al., 2021). A dash-cam can be mounted on a vehicle and pavement surface images can be obtained as vehicle moves along the road.

4.3.4 Satellite

The human eye cannot see the light beyond the visible spectrum. Satellite images have the potential to derive the physical and chemical properties of materials as they can detect wavelengths in a wide range of the spectrum. The advantage of these methods is collecting high resolution images without interrupting traffic flow (Schnebele et al., 2015). Despite the non-deniable advantages of satellite platforms for providing vast regional information in a single image, data collection and their application can be limited by atmospheric inferences and temporal and spatial resolutions (Job, 2021). Satellite images consist of bands and pixels in which each pixel has a number referred to as Digital Number (DN) or Brightness Value (BV). Figure 24 shows a remotely sensed image and the pixels corresponding brightness values ranging from 0 to 255. Every material has a specific spectral response that can be used for land use/ land cover classification. The brightness values in a remotely sensed image can provide useful information for assessing the present situation.

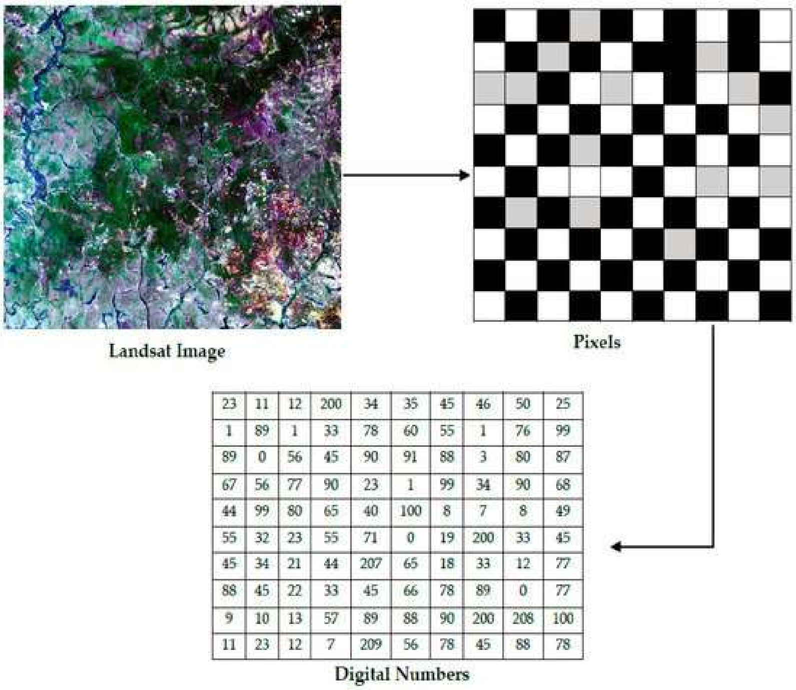

23	11	12	200	34	35	45	46	50	25
1	89	1	33	78	60	55	1	76	99
89	0	56	45	90	91	88	3	80	87
67	56	77	90	23	1	99	34	90	68
44	99	80	65	40	100	8	7	8	49
55	32	23	55	71	0	19	200	33	45
45	34	21	44	207	65	18	33	12	77
88	45	22	33	45	66	78	89	0	77
9	10	13	57	89	88	90	200	208	100
11	23	12	7	209	56	78	45	88	78

Figure 24. Pixels and their corresponding brightness values of a satellite image (Phiri & Morgenroth, 2017).

4.4 Data Acquisition

The satellite images used for this study should be the most cost-effective, suitable, and accessible dataset with a high spatial resolution to distinguish roads and their surroundings. There are numerous satellite platforms each providing a wide range of imagery datasets with various features for different monitoring applications. However, based on the preliminary analysis results, the remote sensing satellite sensors considered for this study include Sentinel-2 and PlanetScope as multispectral remote sensing platforms.

4.4.1 Sentinel-2 Satellite

Sentinel-2 is the most recent Earth observation mission of the European Space Agency (ESA) utilized for monitoring land, vegetation, water, and coastal areas. Sentinel-2 includes Sentinel-2A and Sentinel-2B satellites launched in June 2015 and March 2017, respectively (Thanh & Kappas, 2017). The twin polar-orbiting Sentinel-2 system includes 13 spectral bands in the visible near-infrared (VNIR) and short-wave infrared (SWIR) spectral ranges with three different spatial resolutions of 10, 20, and 60 m. The temporal resolution (revisit time) is five days, making the Sentinel one of the highest frequency satellites (Traganos & Reinartz, 2018). In this study, Sentinel-2 Level-1C low cloud cover (atmospherically corrected) images are downloaded from the ESA Copernicus Open Access Hub, which provides freely available multispectral multitemporal imagery data from the globe. After logging in to the Open Hub platform, the date, sensor, and product level need to be determined. Then, by drawing the rectangular box over the study area, the engine will start searching for the results. The overlapping images between selected dates will display. Figure 25 displays the acquired results and the overlapping images for Atlanta metropolitan area from the Sentinel-2 satellite.

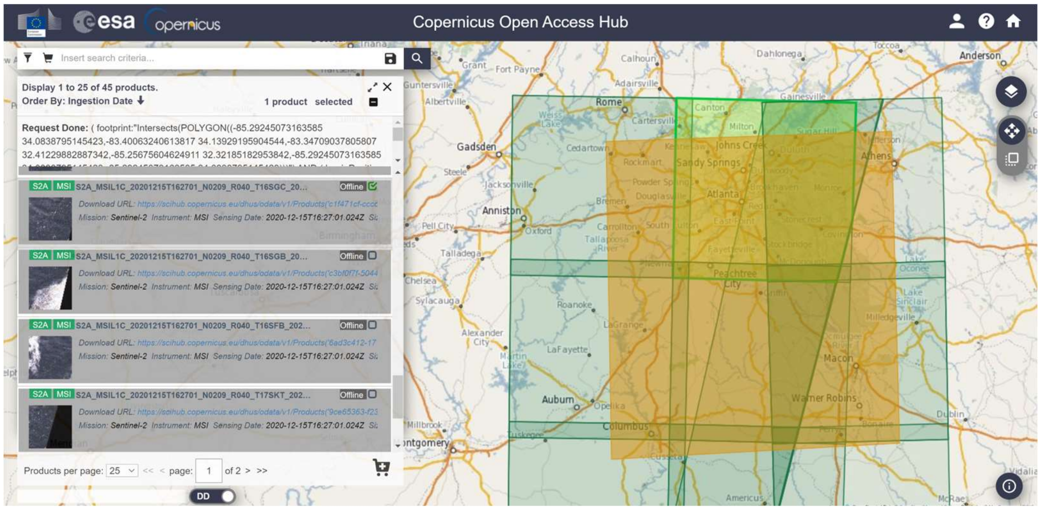

Display 1 to 25 of 45 products.
Order By: Ingestion Date ↓
1 product selected

Request Done: (footprint:"Intersects(POLYGON((-85.29245073163585 34.0838795145423,-83.40063240613817 34.13929195904544,-83.34709037805807 32.41229882887342,-85.25675604624911 32.32185182953842,-85.29245073163585

S2A MSI S2A_MSIL1C_20201215T162701_N0209_R040_T16SGC_20... Offline ☑
Download URL: https://scihub.copernicus.eu/dhus/odata/v1/Products('c1f471cf-cccc
Mission: Sentinel-2 Instrument: MSI Sensing Date: 2020-12-15T16:27:01.024Z

S2A MSI S2A_MSIL1C_20201215T162701_N0209_R040_T16SGB_20... Offline ☐
Download URL: https://scihub.copernicus.eu/dhus/odata/v1/Products('c3bf0f7f-5044
Mission: Sentinel-2 Instrument: MSI Sensing Date: 2020-12-15T16:27:01.024Z

S2A MSI S2A_MSIL1C_20201215T162701_N0209_R040_T16SFB_202... Offline ☐
Download URL: https://scihub.copernicus.eu/dhus/odata/v1/Products('6ad3c412-17
Mission: Sentinel-2 Instrument: MSI Sensing Date: 2020-12-15T16:27:01.024Z

S2A MSI S2A_MSIL1C_20201215T162701_N0209_R040_T17SKT_202... Offline ☐
Download URL: https://scihub.copernicus.eu/dhus/odata/v1/Products('9ce65363-f23
Mission: Sentinel-2 Instrument: MSI Sensing Date: 2020-12-15T16:27:01.024Z

Figure 25. Sentinel-2 Satellite data acquisition.

4.4.2 PlanetScope Imagery

PlanetScope constellation provides high spatial resolution (3.0 m), highest frequency, and global coverage images (Wu et al., 2021). Planet also provides 50 cm spatial resolution images collected since June 2020, which are not freely available. The surface reflectance base maps are products of PlanetScope imagery with four spectral bands (i.e., blue, green, red, and near-infrared (NIR)). The Planet base maps are comprehensive, have high spatial resolution and frequency, and are atmospherically corrected (cloud-free) and analysis-ready mosaics for better reflection of the ground truth data and further spectral analysis. The imagery type is selected as surface reflectance base maps by defining the coverage area. Then, the date range is selected between quarterly, monthly, or weekly. Finally, the delivery type is selected between web streaming or download. Figure 26 shows the downloaded PlanetScope imagery product from the study area.

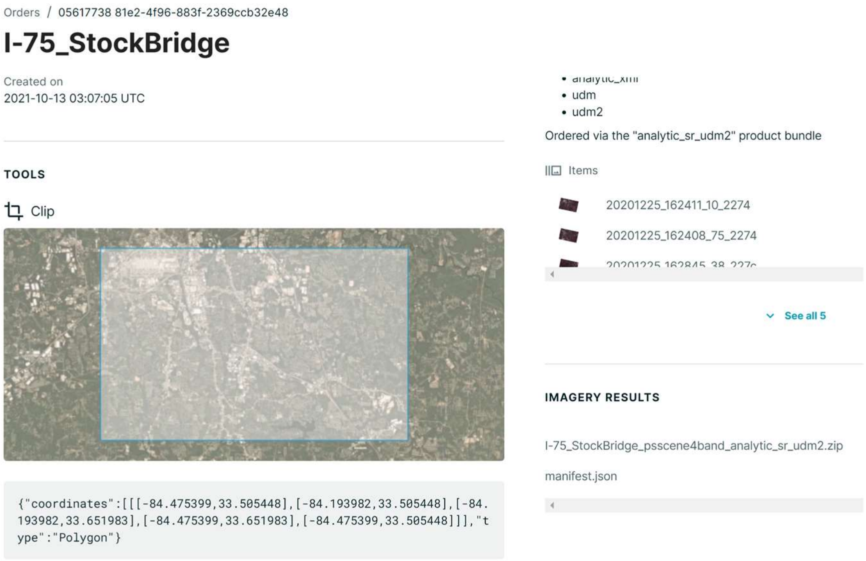

Orders / 05617738 81e2-4f96-883f-2369ccb32e48

I-75_StockBridge

Created on
2021-10-13 03:07:05 UTC

TOOLS

Clip

```
{"coordinates":[[[-84.475399,33.505448],[-84.193982,33.505448],[-84.
193982,33.651983],[-84.475399,33.651983],[-84.475399,33.505448]]],"t
ype":"Polygon"}
```

- analytic_xml
- udm
- udm2

Ordered via the "analytic_sr_udm2" product bundle

Items

20201225_162411_10_2274
20201225_162408_75_2274
20201225_162845_38_227c

See all 5

IMAGERY RESULTS

I-75_StockBridge_psscene4band_analytic_sr_udm2.zip

manifest.json

Figure 26. PlanetScope imagery data acquisition.

4.5 Data Analysis

The Sentinel Application Platform (SNAP) is utilized to locate the data points using the Lat/Long information and then extract the spectrum values of individual pixels from the downloaded imagery datasets. Various pavement sections were investigated by analyzing the reflectance values of their satellite images and corresponding international roughness index (IRI) measurements in different years. For example, Figure 27 illustrates the average spectrum values of three pavement sections located on I-85, I-285, and I-20 in Georgia from 2018 to 2020. Also, Table 17 shows the IRI values for the sections mentioned above provided by the GDOT. As seen in the figure, there is no significant difference between the reflectance values of different pavement sections over the years. For example, the spectral view of the I-20 and I-285 sections in 2019 and 2020 are almost identical. The IRI index typically presents the smoothness and ride quality of the roadway segment (Arhin & Noel, 2014). The higher IRI value indicates a rough pavement.

Based on the data from Table 17, the IRI value of the section located on I-85 in 2020 is higher than the other two years. Thus, its surface reflectance value is supposed to be higher, while the spectrum view in Figure 27 does not reflect the idea.

Although Sentinel-2 imagery benefits from higher radiometric resolution (Razzak et al., 2021), the extracted data does not provide a reasonable accuracy due to the medium spatial resolution of images. Thus, the mixed pixel issue occurs because extracting the pure reflection value of pixels is not feasible. In other words, the pixels of the study area (road sections) are mixed with the adjacent area (usually road shoulders). Therefore, there is often more than one class type within a pixel, making the extraction of reflectance values complicated (Dey et al., 2009 and Yang et al., 2021). Figure 28 shows the mixed pixel issue because of the low resolution of the Sentinel-2 images. As seen in the figure, the pins should represent only the road surface while most present the road shoulder's reflectance values. That is why Sentinel-2 imagery fails to investigate the relationship between degradation/ oxidation of asphalt pavements and change in brightness values.

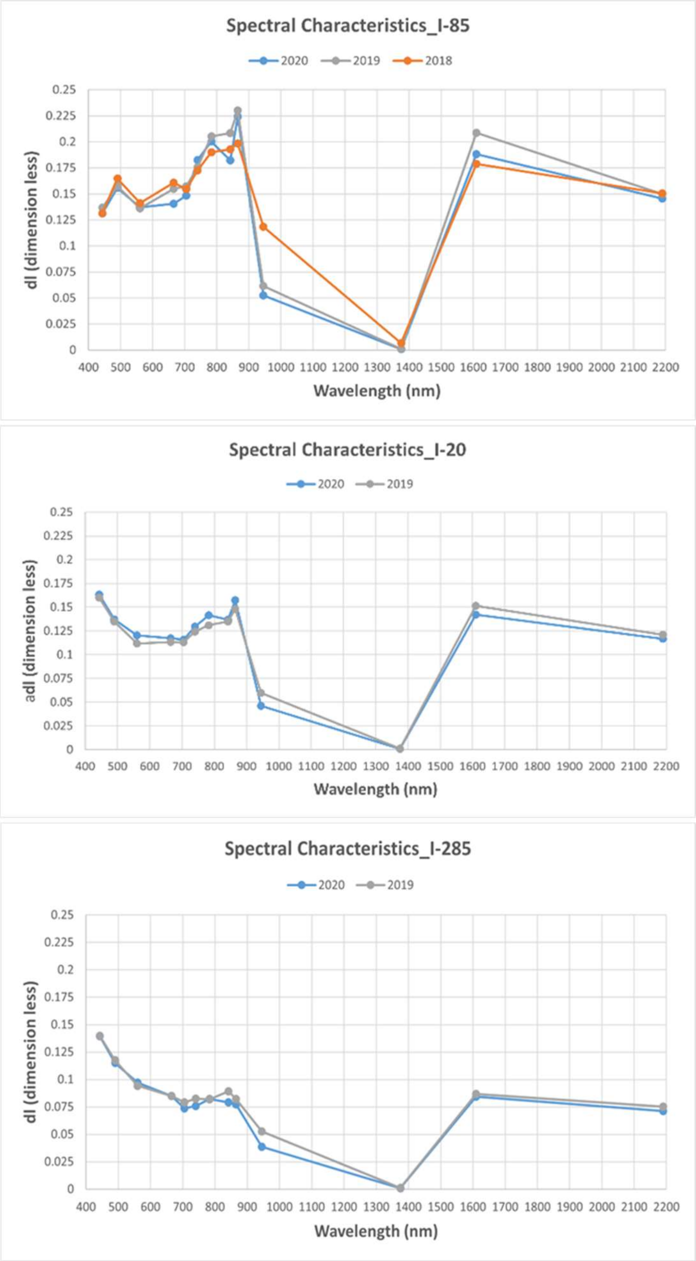

Figure 27. Spectral characteristics of Georgia pavement roads in Sentinel-2 satellite images.

Table 17. Measured IRI values for different pavement sections.

I-85	
SurveyDate	IRI
09/05/18	**88.8**
06/16/19	**97.1**
05/30/20	**99.5**
I-20	
07/24/19	**245.9**
05/04/20	**203.3**
I-285	
11/29/19	**64.3**
05/08/20	**53.5**

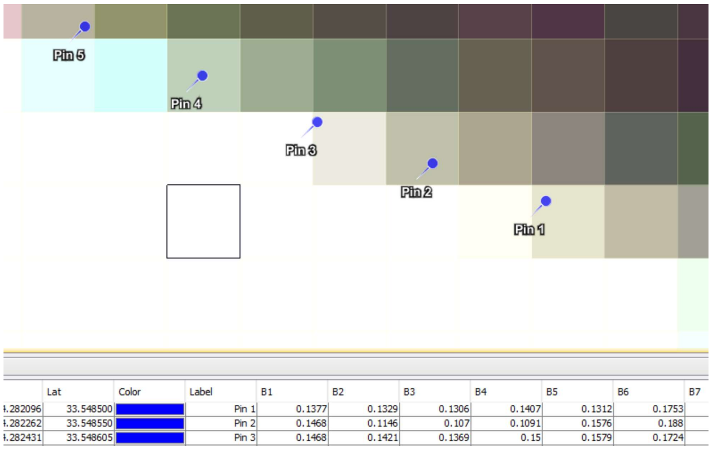

	Lat	Color	Label	B1	B2	B3	B4	B5	B6	B7
.282096	33.548500	🟦	Pin 1	0.1377	0.1329	0.1306	0.1407	0.1312	0.1753	
.282262	33.548550	🟦	Pin 2	0.1468	0.1146	0.107	0.1091	0.1576	0.188	
.282431	33.548605	🟦	Pin 3	0.1468	0.1421	0.1369	0.15	0.1579	0.1724	

Figure 28. Mixed pixel issue observed in Sentinel-2 images.

As a result, the Planet's atmospherically corrected and ready to use base-maps are considered for further analysis. As mentioned, the Planet's surface reflectance base maps have four spectral bands. Thus, there are four band reflection values for each pixel of the surface images, as shown in Figure 29. The 600 pins from the asphalt pavement sections of I-75 are found using their Lat/ Long information, and the reflectance values of the four bands are extracted.

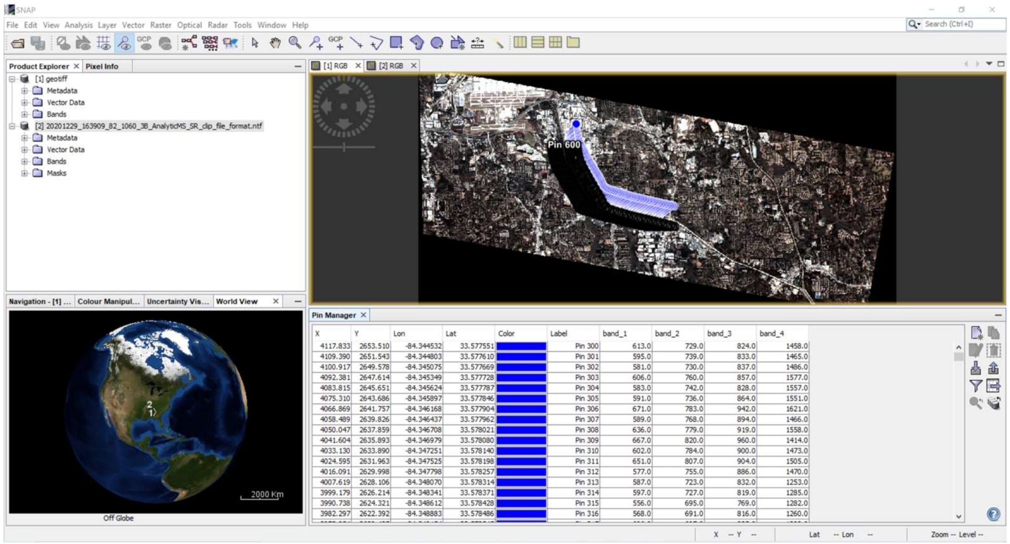

X	Y	Lon	Lat	Color	Label	band_1	band_2	band_3	band_4
4117.833	2653.510	-84.344532	33.577551	🟦	Pin 300	613.0	729.0	824.0	1458.0
4109.390	2651.543	-84.344803	33.577610	🟦	Pin 301	595.0	739.0	833.0	1465.0
4100.917	2649.578	-84.345075	33.577669	🟦	Pin 302	581.0	730.0	837.0	1486.0
4092.381	2647.614	-84.345349	33.577728	🟦	Pin 303	606.0	760.0	857.0	1577.0
4083.815	2645.651	-84.345624	33.577787	🟦	Pin 304	583.0	742.0	828.0	1557.0
4075.310	2643.686	-84.345897	33.577846	🟦	Pin 305	591.0	736.0	864.0	1551.0
4066.869	2641.757	-84.346168	33.577904	🟦	Pin 306	671.0	783.0	942.0	1621.0
4058.489	2639.826	-84.346437	33.577962	🟦	Pin 307	589.0	768.0	894.0	1466.0
4050.047	2637.859	-84.346708	33.578021	🟦	Pin 308	636.0	779.0	919.0	1558.0
4041.604	2635.893	-84.346979	33.578080	🟦	Pin 309	667.0	820.0	960.0	1414.0
4033.130	2633.890	-84.347251	33.578140	🟦	Pin 310	602.0	784.0	900.0	1473.0
4024.595	2631.963	-84.347525	33.578198	🟦	Pin 311	651.0	807.0	904.0	1505.0
4016.091	2629.998	-84.347798	33.578257	🟦	Pin 312	577.0	755.0	886.0	1470.0
4007.619	2628.106	-84.348070	33.578314	🟦	Pin 313	587.0	723.0	832.0	1253.0
3999.179	2626.214	-84.348341	33.578371	🟦	Pin 314	597.0	727.0	819.0	1285.0
3990.738	2624.321	-84.348612	33.578428	🟦	Pin 315	556.0	695.0	769.0	1282.0
3982.297	2622.392	-84.348883	33.578486	🟦	Pin 316	568.0	691.0	816.0	1260.0

Figure 29. Spectrum value extraction using the SNAP software.

4.6 Discussion

Remote sensing technology offers non-destructive and non-intrusive approaches to replacing existing traditional pavement survey methods and serves the needs of transportation engineers. In this study, Sentinel-2 and PlanetScope satellite images were utilized to investigate the relationship between the pavement surface color change (due to the oxidation of the asphalt material) and the need for maintenance of the Georgia roads on time. The IRI values were also considered to correlate with the reflectance values obtained from the satellite images. The results indicate that the differences between the spectrum view of the pavement sections over the years are negligible. Also, there is no apparent relationship between the IRI indices and the corresponding reflectance values. The Sentinel-2 satellite images have a medium spatial resolution that cannot capture the pavement surface changes due to the distresses over time. PlanetScope images, on the other hand, have lower radiometric resolution with only four bands in the visible and near-infrared, which are not sufficient for observing the spectral characteristics of the pavement surface changes. Moreover, the annual average rainfall in Georgia is very high, and floods are common in the state. Thus, rain is another factor challenging the idea of finding the relationship between the color change of asphalt pavements and their deterioration. After the rain, the pavement color remains dark until the surface dries up completely. Additionally, obtaining cloud-free satellite images on a specific date/time is demanding since Sentinel-2 images are not atmospherically corrected. Thus, the satellites' revisit time and the usual cloudy sky of Georgia might occur simultaneously, resulting in highly cloud-covered images from the area, making the transport infrastructure observation challenging.

CHAPTER 5

5. A DEEP LEARNING APPROACH FOR PAVEMENT CRACK IDENTIFICATION PURPOSES

5.1 Problem Statement

Cracking is usual damage in asphalt pavements and an essential factor to be considered in the accurate assessment and maintenance phase. Recent advancements and technologies in image processing have benefited highway specialists in diagnosing pavement distresses and acting on time. As a result, deep learning methodologies are being applied extensively to pavement crack detection and segmentation (Feng et al., 2020). As discussed in the previous chapter, due to the continuous nature of data acquisition in remote sensing approaches, satellite imageries have the potential to be utilized for transportation assessment purposes. However, the remote sensing approach fails to provide an indication for oxidation, degradation, and distress of the asphalt pavement sections in Georgia due to the low spatial resolution of the freely accessible satellite images. Therefore, we decided to utilize our image datasets taken from the Georgia pavement surfaces using a moving vehicle. The dataset is then processed to be fed into a deep learning-based model to detect cracks and distresses.

The following section presents a literature review to discuss the state-of-the-art image processing techniques applied in pavement crack detection.

5.2 Machine Learning Methodologies in Pavement Assessment

In the last few years, numerous studies have employed deep learning methodologies and shown the usefulness and cost-effectiveness of these techniques in infrastructure monitoring. However, there are pros and cons with every single model. Some of the developed architectures in pavement crack detection using image processing algorithms are discussed below.

An Automated Pavement Imaging Program (APIP) was conducted by Mustaffar et al. (2008) to evaluate pavement distress conditions. The dataset consists of images taken by a digital camera with its axis perpendicular to the road surface. The automated program classifies longitudinal, transverse, and alligator cracks and finally estimates pavement distress severity with an accuracy of about 90 percent. CrackNet is a deep learning-based pavement crack detection software with high precision. Zhang et al. (2018) developed an improved software architecture called CrackNet II for enhanced learning capability and faster performance. The proposed algorithm has a deeper architecture with more hidden layers and fewer parameters resulting in five times faster performance than the original assessment model. Fan et al. (2018) proposed a supervised methodology based on deep learning, which can detect cracks in the raw images without the need for preprocessing. In this method, small patches from crack images are extracted as inputs for generating a dataset and training the crack detection model. Inkoom et al. (2019) investigated the application of recursive partitioning and artificial neural networks in predicting the pavements crack rating. In this study, explanatory variables such as the average daily traffic, truck factor, asphalt thickness, roadway functional classification, and pavement condition time series are utilized in the model. Based on the results, the model can be adopted by DOTs to predict highway cracking conditions' performance effectively Hoang and Nguyen (2019) developed a novel and automated model for asphalt pavement crack classification based on machine learning and image processing. In this method, different feature selection scenarios are utilized to create datasets from digital images. The datasets are then utilized for training and verifying the machine learning algorithms, including the random forest (RF), the artificial neural network (ANN), and the support vector machine (SVM). The proposed method can assist transportation agencies with a high classification accuracy rate. Tsai et al. (2021) developed an accurate raveling detection and classification algorithm using 3D pavement data to overcome the inefficiencies of the traditional raveling survey methods in the state DOTs. In this study, 3D pavement data was collected on state roads of Georgia for training and testing. Then, three supervised machine learning techniques, including AdaBoost, support vector machine (SVM), and random forests, were used for the detection and classification of raveling in the dataset. Kyriakou et al. (2021) also developed a data-driven framework using artificial neural networks, supervised machine learning methods, and smartphone technology for the spatial condition- assessment mapping of surface anomalies of pavements. The study offers easy, safe, low-cost, and continuous detection of road anomalies for highway specialists. Traditional crack detection models have difficulties such as low efficiency and missing detection. Hu et al. (2021) used YOLOv5 series detection models to overcome these problems and automatically detect cracks with high speed and accuracy. YOLO (You Only Look Once) is one of the fastest real-time object detection algorithms, which has been modified to the latest version named YOLOR; You Only Look One Representation. YOLO is called an object detector as the algorithm finds the location (the boundary box of objects) as well as the class of objects. The algorithm, based on the latest generation of Deep Neural Network (DNN) architecture, takes only one single forward propagation through a neural network to detect objects, thus known for its speed and high accuracy (Menghini et al., 2021). This model architecture utilizes regression to provide the class probabilities of the detected images (Redmon et al. 2016) and employs both implicit and explicit knowledge simultaneously to the model training so the model can learn various tasks through this general representation (Zhang et al. 2021 and Redmon et al. 2016). YOLOR divides the individual input images into an even number of grids. If the center of a detected object falls into a grid cell, that grid cell must detect the object. That is, YOLOR predicts bounding boxes, the confidence of those bounding boxes, and their class probabilities at the same time (Redmon et al., 2016). It can be concluded that YOLOR has advantages over traditional object detection methods as it is extremely fast so that the frames of a streaming video can be processed in real-time. Second, YOLOR takes the entire image in the training and testing steps. Thus, it has fewer background errors compared to Fast R-CNN. Third, YOLOR learns how to generalize the representations of objects. Thus, the model performs well when applied to new domain inputs (Redmon et al., 2016). The widespread use of smartphones for pavement crack detection provides an easier and less expensive method for collecting data. However, their lower quality entails in failure of traditional models for accurate crack detection. Huyan et al. (2020) developed a state-of-the-art pixel-wise crack detection architecture called CrackU-net, which utilizes convolution, pooling, transpose convolution, and concentration operations and yields high accuracy and precision.

This study utilizes a semantic segmentation model called SegNet for pavement crack identification purposes. In the following section, the architecture of the SegNet is discussed in detail.

5.3 Pavement Crack Identification Network Using SegNet Architecture

SegNet is a pixel-wise semantic segmentation algorithm that consists of an encoder network with 13 layers, a corresponding 13-layer decoder network followed by a final pixel-wise classification layer. The decoder network is responsible for mapping the low-resolution encoder feature maps to full input resolution feature maps. The encoder extracts low-resolution feature maps, and then the decoder maps them to full-input-resolution features using max-pooling indices. The output of the final decoder is then passed to a trainable multi-class SoftMax classifier to produce class probabilities for individual pixels (Badrinarayanan et al., 2017). SegNet has no fully connected layers. That is the reason why it can accept images of arbitrary size as input (Chen et al., 2020). Also, the algorithm is proved to be efficient in terms of memory and computational time by using an efficient weight update technique called stochastic gradient descent (SGD) (Badrinarayanan et al., 2017). Gradient Descent is a standard optimization algorithm based on minimizing the sum of squared errors. However, this algorithm has a high chance of getting into the local minima trap. To avoid this problem, Stochastic Gradient Descent (SGD) introduces the randomness factor in estimating every observation, which considerably increases the chance of finding the global minimum (i.e., the most optimum solutions).

The CamVid dataset has been utilized for training the SegNet model. The Cambridge-driving Labeled Video Database (CamVid) is a collection of videos with object class semantic labels. The dataset includes 32 semantic classes with ground truth labels for each pixel (Brostow et al., 2009). Our own collected dataset (images with pavement cracks) is used in in this research study to fine-tune the model. In addition, we needed to customize the model so that the number of classes to be predicted matches the number of classes in the pavement crack dataset. Finally, the network is being trained to update the weights of the model.

The objects in the original training data (CamVid) and the pavement cracks in the new dataset are entirely different from each other and cannot share common characteristics. As a result, we are leveraging the transfer learning approach to be able to fit a well-performing model into this domain.

Transfer Learning is the methodology in which high-performing trained models are reused to perform on the data from another domain (Weiss et al., 2016). Since developing a powerful deep learning model from scratch is computationally expensive and time-consuming, transfer learning is considered an acceptable alternative approach widely used in training CNN models. Therefore, pre-trained models with fine-tuned weights and parameters are used as feature extractors (Chen et al., 2020). Depending on the size of the new dataset and its similarity to the original dataset, the approach for using transfer learning will be different.

In most cases, transfer learning is not easily applicable, and there is a need for fine tuning. Fine tuning is the idea of adjusting the parameters and the weights associated with each node in the deep learning layers to customize the initial model based on the new dataset (Käding et al., 2016). One of the primary elements to be fine-tuned in each specific application is finding the optimum learning rate. Learning rate is a value that controls how many updates should be applied to adjust the model weights in response to the errors in each iteration of the learning process (Gotmare et al., 2018). One of the common issues in model training is being too sensitive to all variations in the features of training data which leads to overfitting. Overfitting happens when the model becomes too specific and fails to perform well on the unseen data. Learning rate can overcome this shortcoming by providing a threshold for weight adjustments with respect to the loss functions (Li H. et al., 2019). The learning rates considered in our model are set to 0.01 and 0.005.

Our model is being trained and validated using a public dataset in this domain (Khan Ha, 2020). The dataset consists of more than 3,000 images with different pavement cracks and their corresponding annotations. For testing purposes, we used pavement surface images collected through a drive-by sensing approach from the Georgia interstate roads, which were fully unseen to the model, to predict the cracks within each individual image.

Drive-by sensing is a data collection paradigm in which vehicle-borne sensors keep recording data from the target phenomena. This sensing approach is cost-efficient and a great choice when target properties, in our case, asphalt quality, are dynamic (Anjomshoaa et al., 2018). For example, public transportation vehicles provide an excellent infrastructure to collect data continuously as they are wandering around cities (Lee & Gerla, 2010). To be more specific, since pavements are the primary land covers for vehicles movement, drive-by sensing is a perfect match for continuous pavement quality monitoring.

In this study, we leveraged drive-by sensing using a GPR scan vehicle at the University of Georgia. The following section covers the details of the data collection and preparation.

5.4 Dataset Collection and Preparation

In this study, a GPR scan vehicle is used to take images from the state of Georgia's pavement roads, as shown in Figure 30. On-dash mounted camera is utilized to capture images as the vehicle moves on the road. As shown in Figure 31, the front view images with complex backgrounds are recorded to evaluate the surface conditions of the road sections. The complex background includes lane lines, small trash, and oil/ water stains. It should be noted that only the rightmost lane is covered in each surface image. When taking images, the latitude and longitude information of the road sections are also recorded using a Global Positioning System (GPS).

Figure 30. UGA GPR van.

Figure 31. UGA road survey control units.

The critical state routes of District 7 in the Atlanta Metropolitan area from which the images are taken are I-20, I-75, I-85, I-285, I-675, GA-3, GA-5, and GA-400.

The acquired images from the Georgia roads are captured by a camera with less than 2-megapixel resolution (image dimensions: 1548 x 1155). To be able to feed the model with the dataset, the images are cropped to 448 by 448 pixels. Cracks of all images are manually labeled using an open-source and pixel-wise annotating platform called Label Studio. Thus, there are annotated images corresponding to the individual raw images with the same name in the dataset. Figure 32 shows a sample image taken from our vehicle-borne data collection.

Figure 32. Sample image taken from the Georgia roads.

5.5 Experimental Environment

In this study, we used PyTorch as the machine learning framework to implement our customized deep learning model. PyTorch is a framework primarily developed by Meta AI that enables arithmetic operations with powerful acceleration through graphics processing units (GPUs). On the other hand, for the hardware environment, we utilized Google Colaboratory (Colab) notebooks, an interactive environment on the Google cloud platform that leverages cloud-based GPUs to train and evaluate deep learning models. All the model training, fine-tunings, evaluation, and testing in this chapter are being performed using PyTorch on Google Colab.

5.6 Performance Evaluation

After training the model, the new weights are recorded. These weights are further used to test the unseen images to predict the cracks. In the training phase, we applied different numbers of epochs to find the optimum parameter weights. In neural network algorithms, an epoch represents a complete pass through the training data. The model parameters and weights associated with each layer are updated through each epoch. The number of epochs is one of the essential factors that leads to appropriately trained models. The number of epochs considered in this model are 10, 50, and 100. Also, the cross-entropy loss is the metric to measure how well the customized model performs the classification task at the end of each epoch. This metric evaluates the performance of classification models that have the output in terms of probability.

In this study, we consider precision, recall, and IoU (intersection over union) to evaluate the performance of the proposed crack identification network. Precision represents the ratio of the number of positive samples that are correctly classified to the total number of samples that are classified as positive (might be either positive, i.e., true positive, or negative, i.e., false positive) (Kane, 1996). The recall is a metric that identifies the proportion of actual positive values correctly. In other words, it is the fraction of true positives over the summation of true positives and false negatives (Buckland & Gey, 1994). Intersection over Union (IOU) is an evaluation metric to describe the extent of overlap between two specific sections. Intersection over Union measures the accuracy of an object detection model on a specific dataset. A high IOU shows a great overlapping region in the images of the dataset (Rezatofighi et al., 2019). The F1-score values are also calculated. F1-score is a commonly used metric in classification models (Lipton et al., 2014). Since the F1-score is an average of precision and recall, it is sometimes convenient to have only one performance metric rather than multiple. Moreover, the average loss values are provided at the end of each epoch to see how the model is training.

5.7 Results

The performance evaluation metrics are reported across the test images in the form of a tensor after the model evaluation is completed. Table 18 shows the metrics for each learning rate and different number of epochs. Since there are two classes/objects in our case, each tensor represents the corresponding value for each class. For example, for learning rate of 0.01 with 10 epochs, precision: tensor ([0.99, 0.33]) indicates that for each pixel predicted to be part of the pavement surface, how many pixels are part of the pavement surface which equals 99.0%. Similarly, the precision for pavement cracks equals 33.0%. The same scenario applies to recall and IoU. The recall value for pavement surface is 97.0%, while the same metric for crack equals 87.0%. Finally, the IoU for pavement surface is equal to 97.0%, whereas the same metric for crack equals 48.0%. Figures 33-35 illustrate the test images for learning rate of 0.01 after 10, 50, and 100 epochs. As seen in the figures, our model can predict the cracks after ten epochs. However, there are some spots which classified as cracks by mistake. Also, there are cracks that the model has not identified. As the number of epochs increases, the model performs better. Figure 34 shows the same test images after the model evaluation and 50 epochs of training. As seen in the figure, crack detection performs much better in comparison to the lower number of epochs. The results in Table 18 indicate that the model performs better when learning rate is 0.01 than 0.005. Considering the fact that detecting all of the cracks in test images are crucial, the recall is the most important metric. The recall measurement has the maximum value for either pavement surface or cracks when learning rate is 0.01 and number of epochs is equal to 100. Also, the F1-score is maximum in either pavement surface or crack detection task when learning rate is equal to 0.01. Thus, it can be concluded that the optimum number of epochs for our model equals 100 with learning rate of 0.01.

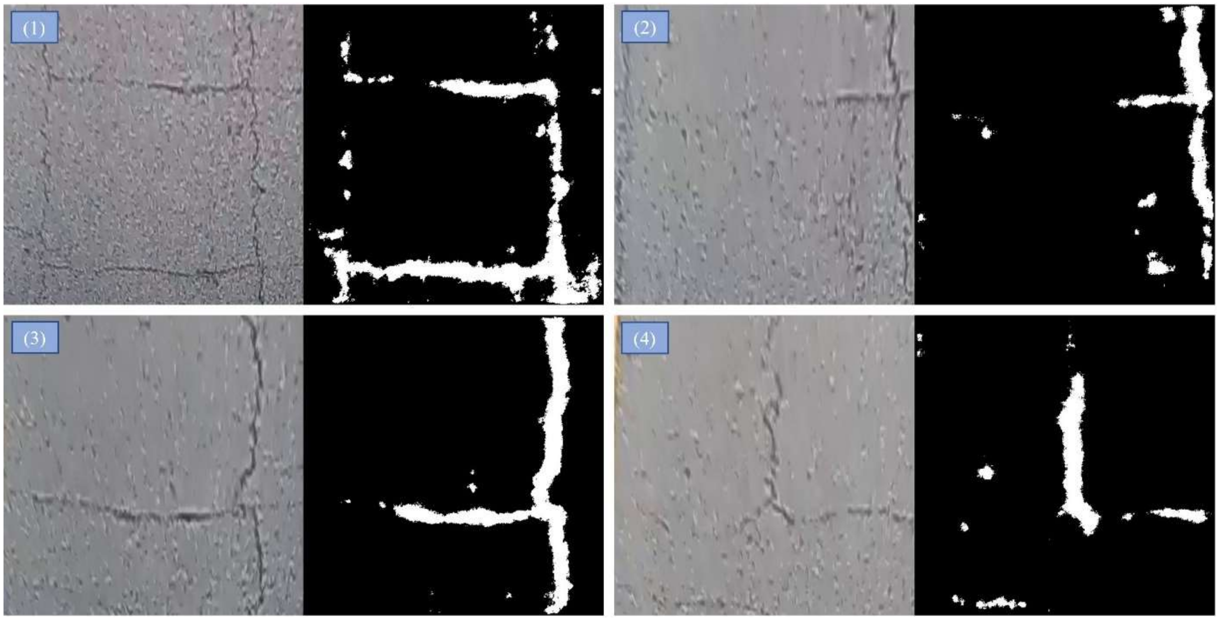

Figure 33. Test images after 10 epochs.

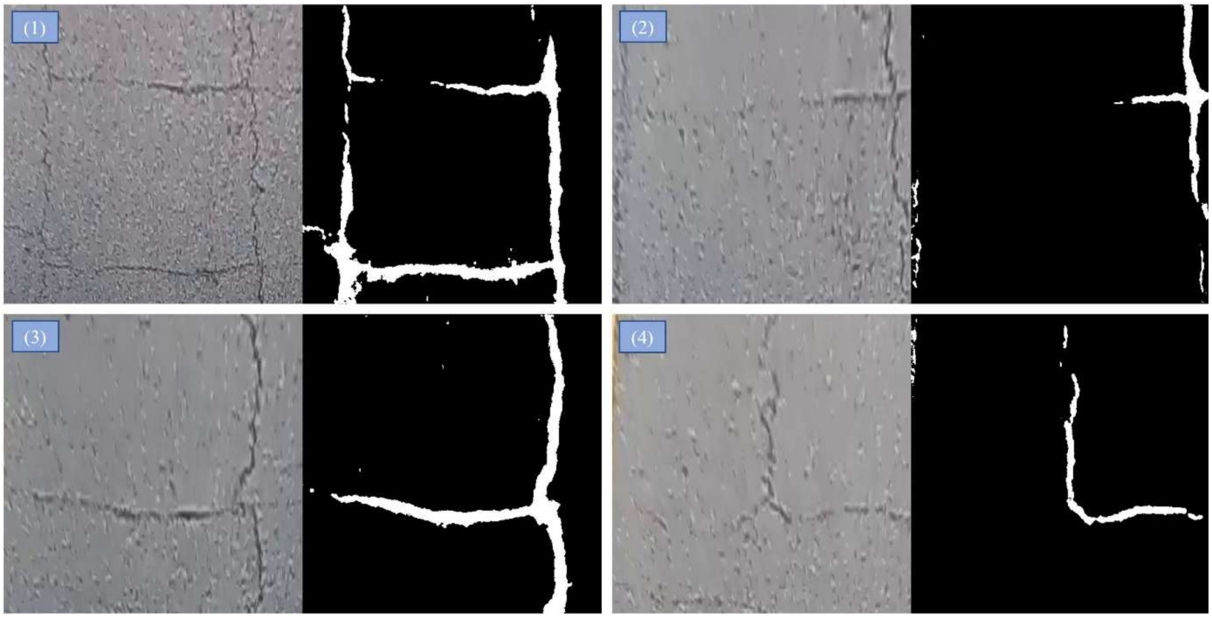

Figure 34. Test images after 50 epochs.

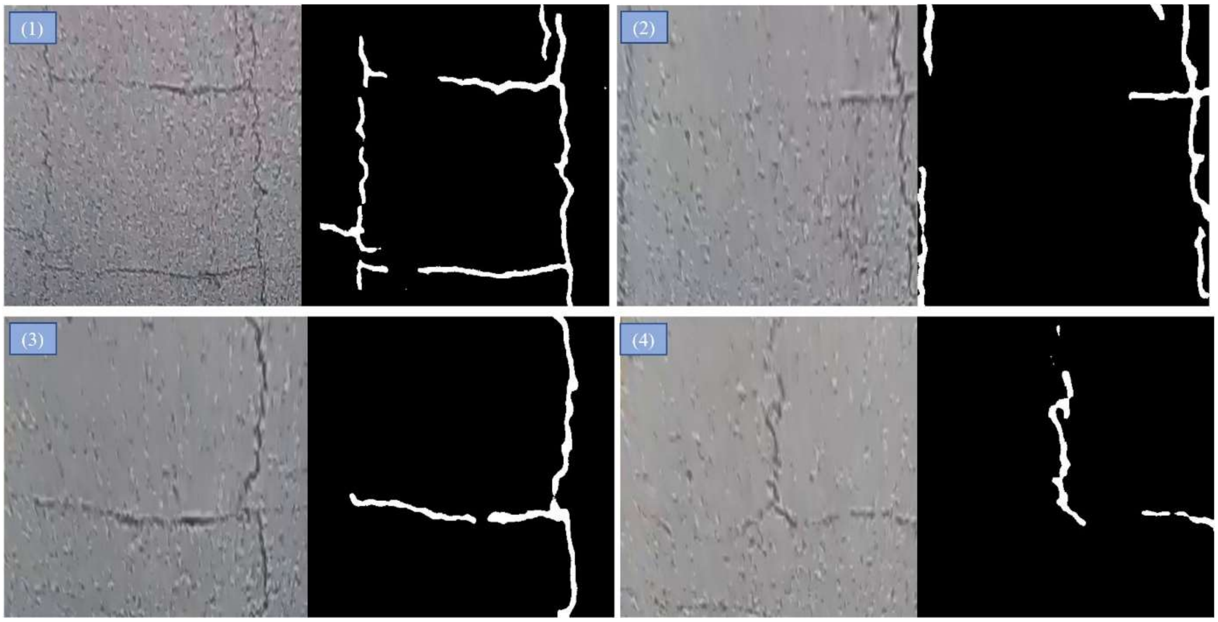

Figure 35. Test images after 100 epochs.

Table 18. Performance evaluation metrics.

No. Epochs	Precision	Recall	F1-Score	Intersection over Union (IoU)	Average Loss
Learning Rate: 0.01					
10	[0.99, 0.33]	[0.97, 0.89]	[0.98, 0.48]	[0.97, 0.31]	0.090
50	[0.99, 0.52]	[0.99, 0.89]	[0.99, 0.66]	[0.99, 0.49]	0.081
100	[0.99, 0.59]	[0.99, 0.91]	[0.99, 0.72]	[0.99, 0.57]	0.080
Learning Rate: 0.005					
10	[0.99, 0.46]	[0.99, 0.59]	[0.99, 0.52]	[0.98, 0.32]	0.091
50	[0.99, 0.42]	[0.98, 0.94]	[0.98, 0.58]	[0.98, 0.41]	0.082
100	[0.99, 0.58]	[0.99, 0.89]	[0.99, 0.70]	[0.99, 0.54]	0.080

To estimate the dimensions of the detected cracks, the percent of the pavement cracks (white pixels) is calculated by counting the white pixels in the predicted image and dividing by the total number of pixels (448 * 448) in an image. Table 19 shows the number of pixels with cracks and the percent of pavement cracks over the entire image for test images shown in Figures 33-35.

Table 19. Pixel-level information of pavement cracks.

No. Epochs	No. Pixels with Crack	Percent of Pavement Cracks	No. Pixels with Crack	Percent of Pavement Cracks	No. Pixels with Crack	Percent of Pavement Cracks	No. Pixels with Crack	Percent of Pavement Cracks
	Image (1)		**Image (2)**		**Image (3)**		**Image (4)**	
	Learning Rate: 0.01		**Learning Rate: 0.01**		**Learning Rate: 0.01**		**Learning Rate: 0.01**	
10	1386900	6.91%	555990	2.77%	979500	4.88%	487750	2.43%
50	1268500	6.32%	909200	4.53%	842960	4.20%	367350	1.83%
100	1162100	5.79%	881200	4.39%	776800	3.87%	313150	1.56%
No. Epochs	**Learning Rate: 0.005**		**Learning Rate: 0.005**		**Learning Rate: 0.005**		**Learning Rate: 0.005**	
10	1922800	9.58%	909250	4.53%	1075780	5.36%	843970	4.20%
50	1655900	8.25%	1117980	5.57%	961400	4.79%	453700	2.26%
100	1274500	6.35%	927260	4.62%	838950	4.18%	377450	1.88%

CHAPTER 6

6. CONCLUSIONS AND RECOMMENDATIONS

6.1 CONCLUSIONS

In this study, the state-of-the-art machine learning and remote sensing techniques are utilized to monitor and assess the pavement network in the state of Georgia.

First, ESAL factors were updated using the most recent high resolution WIM data. Then, data from WIM stations throughout the state were utilized to develop Georgia-specific TTC groups. Unsupervised learning algorithms were leveraged to analyze high-dimensional traffic characteristic data collected from the existing WIM stations. The performance evaluation results showed that the global default traffic inputs overpredict the pavement distresses compared to the customized TTC groups developed from the state-specific traffic data.

Also, traffic data from recent years were obtained using active CCS and WIM sites throughout the state to capture the change in traffic characteristics over time and to update the lane distribution factors in the Georgia pavement design manual. Based on the results, The truck percentage was proved to be insignificant in determining the LDF values for. Also, the study proved that COVID-19 has not changed Georgia’s LDF pattern significantly. The remote sensing technology was leveraged for infrastructure health monitoring purposes The objective was to correlate the asphalt pavement color change and the best time for performing maintenance without needing an on-site survey which is time-consuming and laborious. The study proved that based on the current technology, remote sensing cannot replace field inspection. However, the spectral signal is an additional level of information that can be considered in other pavement assessment methods. Due to the low spatial and radiometric resolution of the satellite remote sensing imageries, we attempted to utilize vehicle-borne imagery datasets that can be obtained when GPR scanning the Georgia roads. A deep learning-based pixel-wise model is then utilized to detect the pavement cracks in the dataset. The transfer learning and fine-tuning methods were applied to train the model. Based on the results, the model can detect pavement cracks with a high F1-score of 0.99 and 0.72 for pavement surface and cracks, respectively. Therefore, drive-by sensing is a cost-effective and continuous data collection approach for transport infrastructure monitoring since high resolution datasets can be captured easily and freely by moving vehicles throughout the state.

6.2 FUTURE WORK AND RECOMMENDATIONS

Based on the study, it is highly recommended that separate LDF tables are adopted for pavement design, considering the significant roles that the area and facility types play in determining LDF. Also, it is recommended to continuously monitor truck traffic volume for future consideration.

A Hyperspectral Spectroradiometer called superger is being utilized to scan asphalt pavements for capturing the type and aging condition of pavements in a yearly approach. This method can help validate the reflectance values of freely available satellite images with the spectral values obtained from the hyperspectral superger device.

REFERENCES

Abd Mukti, S. N., & Tahar, K. N. (2021). Low altitude multispectral mapping for road defect detection. Geografia, 17(2).

Adlinge, S. S., & Gupta, A. K. (2013). Pavement deterioration and its causes. International Journal of Innovative Research and Development, 2(4), 437-450.

Albright, D., & Blewett, C. (1988). Volume-based model for forecasting truck lane use on the rural interstate. Transportation research record, 1194, 1-5.

Andreou, C., Karathanassi, V., & Kolokoussis, P. (2011). Investigation of hyperspectral remote sensing for mapping asphalt road conditions. International journal of remote sensing, 32(21), 6315-6333.

Anjomshoaa, A., Duarte, F., Rennings, D., Matarazzo, T. J., deSouza, P., & Ratti, C. (2018). City scanner: Building and scheduling a mobile sensing platform for smart city services. IEEE Internet of things Journal, 5(6), 4567-4579.

ARA, Inc. (2004). ERES Consultants Division, Prepared for National Cooperative Highway Research Program, Guide for mechanistic-empirical design of new and rehabilitated pavement structures, Part 2: Design Inputs, Chapter 4: Traffic.

Arhin, S. A., & Noel, E. C. (2014). Predicting pavement condition index from international roughness index in Washington, DC (No. DDOT-RDT-14-03).

Badrinarayanan, V., Handa, A., & Cipolla, R. (2015). Segnet: A deep convolutional encoder-decoder architecture for robust semantic pixel-wise labelling. arXiv preprint arXiv:1505.07293.

Brostow, G. J., Fauqueur, J., & Cipolla, R. (2009). Semantic object classes in video: A high-definition ground truth database. Pattern Recognition Letters, 30(2), 88-97.

Buckland, M., & Gey, F. (1994). The relationship between recall and precision. Journal of the American society for information science, 45(1), 12-19.

Federal Highway Administration (2018). Weigh-in-Motion pocket guide, Part 1: WIM technology, data acquisition, and procurement guide. Publication No. FHWA-PL-18-015.

CHATTERJEE, S., ROY, D., CHAKRABORTY, S., & ROY, S. K. Lane Density as Measure of Effectiveness of Multi lane Indian Highways under Heterogeneous Traffic Conditions.

Chen, T., Cai, Z., Zhao, X., Chen, C., Liang, X., Zou, T., & Wang, P. (2020). Pavement crack detection and recognition using the architecture of segNet. Journal of Industrial Information Integration, 18, 100144.

Chorzepa M., Yang J., Kim S., Durham S., Sinha A., Ma S., and Doker N. (2022) Phase-II Weight-In-Motion (WIM) Data Synthesis and Validation. Georgia Department of Transportation, Project RP 20-04, Final Report, June 2020.

Coifman, B., McCord, M., Mishalani, R. G., & Redmill, K. (2004, January). Surface transportation surveillance from unmanned aerial vehicles. In Proc. of the 83rd Annual Meeting of the Transportation Research Board (Vol. 10, pp. 209-219).

Dey, C., Jia, X., Fraser, D., & Wang, L. (2009, December). Mixed pixel analysis for flood mapping using extended support vector machine. In 2009 Digital Image Computing: Techniques and Applications (pp. 291-295). IEEE.

Edgar, T., & Manz, D. (2017). Research methods for cyber security. Syngress.

Fan, Z., Wu, Y., Lu, J., & Li, W. (2018). Automatic pavement crack detection based on structured prediction with the convolutional neural network. arXiv preprint arXiv:1802.02208.

Federal Highway Administration (FHWA, 2018). “Traffic Data Computation Method” Pocket Guide. FHWA-PL-13-027, U.S. Department of Transportation, Federal Highway Administration, Office of Highway Policy Information.

Federal Highway Administration (FHWA, 2018). “Part 1: WIM Technology, Data Acquisition, and Procurement Guide.” Weigh-in-Motion Pocket Guide. FHWA-PL-17-003, U.S. Department of Transportation, Federal Highway Administration, Office of Highway Policy Information, Washington, DC.

Feng, X., Xiao, L., Li, W., Pei, L., Sun, Z., Ma, Z., ... & Ju, H. (2020). Pavement crack detection and segmentation method based on improved deep learning fusion model. Mathematical Problems in Engineering, 2020.

Fwa, T. F., & Li, S. (1995). Estimation of lane distribution of truck traffic for pavement design. Journal of transportation engineering, 121(3), 241-248.

Garilli, E., Bruno, N., Autelitano, F., Roncella, R., & Giuliani, F. (2021). Automatic detection of stone pavement's pattern based on UAV photogrammetry. Automation in Construction, 122, 103477.Georgia Department of Transportation (GDOT, 2019) Pavement Design Manual, Office of Materials and Research.

Goetz, A. F., Rock, B. N., & Rowan, L. C. (1983). Remote sensing for exploration; an overview. Economic Geology, 78(4), 573-590.

Gotmare, A., Keskar, N. S., Xiong, C., & Socher, R. (2018). A closer look at deep learning heuristics: Learning rate restarts, warmup and distillation. arXiv preprint arXiv:1810.13243.

Haider, S. W., Musunuru, G., Buch, N., Selezneva, O. I., Desaraju, P., & Li, J. Q. (2018). Updated analysis of Michigan traffic inputs for pavement-ME design (No. SPR-1678). Michigan State University. Dept. of Civil and Environmental Engineering.

Haider, S. W., Musunuru, G., Buch, N., Selezneva, O., and Schenkel, J. P. (2019) Updating Traffic Inputs for Use in the Pavement Mechanistic-Empirical Design in Michigan. https://doi.org/10.1177/0361198119849913.

Herold, M. (2004). Understanding spectral characteristics of asphalt roads. National Center for Remote Sensing in Transportation, University of California, Santa Barbara.

Herold, M., & Roberts, D. A. (2005, March). Mapping asphalt road conditions with hyperspectral remote sensing. In Proceedings of URS2005 conference, Phoenix, AZ.

Hoang, N. D., & Nguyen, Q. L. (2019). A novel method for asphalt pavement crack classification based on image processing and machine learning. Engineering with Computers, 35(2), 487-498.

Hrůza, P., Mikita, T., Tyagur, N., Krejza, Z., Cibulka, M., Procházková, A., & Patočka, Z. (2018). Detecting forest road wearing course damage using different methods of remote sensing. Remote Sensing, 10(4), 492.

Hu, G. X., Hu, B. L., Yang, Z., Huang, L., & Li, P. (2021). Pavement Crack Detection Method Based on Deep Learning Models. Wireless Communications and Mobile Computing, 2021.

Huyan, J., Li, W., Tighe, S., Xu, Z., & Zhai, J. (2020). CrackU-net: a novel deep convolutional neural network for pixelwise pavement crack detection. Structural Control and Health Monitoring, 27(8), e2551.

Inkoom, S., Sobanjo, J., Barbu, A., & Niu, X. (2019). Prediction of the crack condition of highway pavements using machine learning models. Structure and Infrastructure Engineering, 15(7), 940-953.

Jasim, A. F., Wang, H., and Bennert T. (2019) Evaluation of Clustered Traffic Inputs for Mechanistic-Empirical Pavement Design: Case Study in New Jersey. https://doi.org/10.1177/0361198119853557.

Jensen, J. R. (2009). Remote sensing of the environment: An earth resource perspective 2/e. Pearson Education India.

J. Golrokh, A., Gu, X., & Lu, Y. (2021). Real-Time Thermal Imaging-Based System for Asphalt Pavement Surface Distress Inspection and 3D Crack Profiling. Journal of Performance of Constructed Facilities, 35(1), 04020143.

JOB, F. R. THE APPLICATION OF REMOTE SENSING IN ROAD PAVEMENT CONDITION SURVEY.

Kane, M. (1996). The precision of measurements. Applied measurement in education, 9(4), 355-379.

Karimzadeh, S., & Matsuoka, M. (2021). Development of Nationwide Road Quality Map: Remote Sensing Meets Field Sensing. Sensors, 21(6), 2251.

Käding, C., Rodner, E., Freytag, A., & Denzler, J. (2016, November). Fine-tuning deep neural networks in continuous learning scenarios. In Asian Conference on Computer Vision (pp. 588-605). Springer, Cham.

Ke, R., Li, Z., Tang, J., Pan, Z., & Wang, Y. (2018). Real-time traffic flow parameter estimation from UAV video based on ensemble classifier and optical flow. IEEE Transactions on Intelligent Transportation Systems, 20(1), 54-64.

Khanh Ha. (2020). Crack Segmentation, available online: https://github.com/khanhha/crack_segmentation#Dataset.

Kim, S. S., Yang, J. J., Durham, S. A., Kim, I. K., & Yaghoubi, N. T. (2021). Determination of Equivalent Single Axle Load (ESAL) Factor for Georgia Pavement Design (No. FHWA-GA-21-1804). Georgia. Dept. of Transporation. Office of Performance-Based Management and Research.

Kim, S., Worthey, H., Brink, W., Von Quintus, H., Durham, S., and Chorzepa, M. (2020). RP 17-18: The GDOT Pavement ME Design User Input Guide, FHWA-GA-20-1718.

Kumar, S. R., & Reddy, K. K. (2014). Lane Distribution Factors–A Case Study on NH7 &NH9. and Infrastructure Development, 249.

Kumar, P., & Thakur, R. S. (2021). Liver disorder detection using variable-neighbor weighted fuzzy K nearest neighbor approach. Multimedia Tools and Applications, 80(11), 16515-16535.

Kyriakou, C., Christodoulou, S. E., & Dimitriou, L. (2021). Spatial Roadway Condition-Assessment Mapping Utilizing Smartphones and Machine Learning Algorithms. Transportation Research Record, 03611981211006105.

Lee, U., & Gerla, M. (2010). A survey of urban vehicular sensing platforms. Computer Networks, 54(4), 527-544.

Li, Q., Wang, K. P., Eacker, M., and Zhang, Z. (2017). Clustering methods for truck traffic characterization in pavement ME design. ASCE-ASME Journal of Risk and Uncertainty in Engineering Systems, Part A: Civil Engineering, 3(2), p.F4016003.

Li, Q. J., Wang, K. P., Qiu, S., Zhang, Z. D., and Moravec, M. (2015). Development of simplified traffic loading for secondary road pavement design. International Journal of Pavement Engineering, 16(2), pp.97-104.

Li, H., Li, J., Guan, X., Liang, B., Lai, Y., & Luo, X. (2019, December). Research on overfitting of deep learning. In 2019 15th International Conference on Computational Intelligence and Security (CIS) (pp. 78-81). IEEE.

Lloyd, S. P. (1957). Least squares quantization in PCM. Technical Report RR-5497, Bell Lab, September 1957.

Lipton, Z. C., Elkan, C., & Narayanaswamy, B. (2014). Thresholding classifiers to maximize F1 score. arXiv preprint arXiv:1402.1892.

Lu, Q., & Harvey, J. T. (2006). Characterization of truck traffic in California for mechanistic–empirical design. Transportation research record, 1945(1), 61-72.

Macioszek, E., & Kurek, A. (2021). Extracting Road Traffic Volume in the City before and during covid-19 through Video Remote Sensing. Remote Sensing, 13(12), 2329.

MacQueen, J. B. (1967). Some methods for classification and analysis of multivariate observations. In L. M. Le Cam & J. Neyman (Eds.), Proceedings of the fifth Berkeley symposium on mathematical statistics and probability (Vol. 1, pp. 281–297). California: University of California Press.

Menghini, L., Bella, F., Sansonetti, G., & Gagliardi, V. (2021, September). Evaluation of road pavement conditions by Deep Neural Networks (DNN): an experimental application. In Earth Resources and Environmental Remote Sensing/GIS Applications XII (Vol. 11863, pp. 159-168). SPIE.

Miller, J. S., & Bellinger, W. Y. (2003). Distress identification manual for the long-term pavement performance program (No. FHWA-RD-03-031). United States. Federal Highway Administration. Office of Infrastructure Research and Development.

Mustaffar, M., Ling, T. C., & Puan, O. C. (2008). Automated pavement imaging program (APIP) for pavement cracks classification and quantification-a photogrammetric approach. The International Archives of the Photogrammetry, Remote Sensing and Spatial Information Sciences, 37(B4), 367-372.

Navalgund, R. R., Jayaraman, V., & Roy, P. S. (2007). Remote sensing applications: an overview. current science, 1747-1766.

Nassiri, S., Bayat, A. and Kilburn, P. (2014). Traffic inputs for mechanistic-empirical pavement design guide using weigh-in-motion systems in Alberta. International Journal of Pavement Engineering, 15(6), pp.483-494.

Oh, J., Walubita, L. F., and Leidy, J. (2015). Establishment of statewide axle load spectra data using cluster analysis. KSCE Journal of Civil Engineering, 19(7), 2083-2090.

Ozden, A., Faghri, A., Li, M., & Tabrizi, K. (2016). Evaluation of Synthetic Aperture Radar satellite remote sensing for pavement and infrastructure monitoring. Procedia Engineering, 145, 752-759.

Pan, Y., Zhang, X., Tian, J., Jin, X., Luo, L., & Yang, K. (2017). Mapping asphalt pavement aging and condition using multiple endmember spectral mixture analysis in Beijing, China. Journal of Applied Remote Sensing, 11(1), 016003.

Peterson, D. (1987). National Cooperative Highway Research Program Synthesis of Highway Practice Pavement Management Practices. No. 135. Transportation Research Board: Washington, DC, USA.

Phiri, D., & Morgenroth, J. (2017). Developments in Landsat land cover classification methods: A review. Remote Sensing, 9(9), 967.

Ramachandran, A.N. (2011). Development of traffic data input resources for the mechanistic empirical pavement design process (No. FHWA/NC/2008-11). North Carolina. Dept. of Transportation.

Redmon, J., Divvala, S., Girshick, R., & Farhadi, A. (2016). You only look once: Unified, real-time object detection. In Proceedings of the IEEE conference on computer vision and pattern recognition (pp. 779-788).

Rezatofighi, H., Tsoi, N., Gwak, J., Sadeghian, A., Reid, I., & Savarese, S. (2019). Generalized intersection over union: A metric and a loss for bounding box regression. In Proceedings of the IEEE/CVF conference on computer vision and pattern recognition (pp. 658-666).

Sayyady, F., Stone, J. R., Taylor, K. L., Jadoun, F. M., and Kim, Y. R. (2009) Clustering Analysis to Characterize Mechanistic-Empirical Pavement Design Guide Traffic Data in North Carolina, Journal of the Transportation Research Board 2160(-1):118-127. DOI:10.3141/2160-13

Schnebele, E., Tanyu, B. F., Cervone, G., & Waters, N. (2015). Review of remote sensing methodologies for pavement management and assessment. European Transport Research Review, 7(2), 1-19.

Selezneva, O. I., Ayers, M., Hallenbeck, M., Ramachandran, A., Shirazi, H., & Von Quintus, H. (2016). MEPDG Traffic Loading Defaults Derived from Traffic Pooled Fund Study (No. FHWA-HRT-13-090). United States. Federal Highway Administration.

Stone, J. R., Kim, Y. R., List, G. F., Rasdorf, W., Fadi, J., Sayyady, F., & Ramachandran, A. N. (2011). Development of traffic data input resources for the mechanistic empirical pavement design process (No. FHWA/NC/2008-11). North Carolina. Dept. of Transportation.

Syakur, M. A., Khotimah, B. K., Rochman, E. M. S., and Satoto, B. D. (2018, April). Integration k-means clustering method and elbow method for identification of the best customer profile cluster. In IOP Conference Series: Materials Science and Engineering (Vol. 336, No. 1, p. 012017). IOP Publishing.

Thanh Noi, P., & Kappas, M. (2017). Comparison of random forest, k-nearest neighbor, and support vector machine classifiers for land cover classification using Sentinel-2 imagery. Sensors, 18(1), 18.

Tosti, F., Gagliardi, V., Ciampoli, L. B., Benedetto, A., Threader, S., & Alani, A. M. (2021, September). Integration of remote sensing and ground-based non-destructive methods in transport infrastructure monitoring: advances, challenges and perspectives. In 2021 IEEE Asia-Pacific Conference on Geoscience, Electronics and Remote Sensing Technology (AGERS) (pp. 1-7). IEEE.

Tarefder, R. and Rodriguez-Ruiz, J. I. (2013). WIM data quality and its influence on predicted pavement performance. Transportation Letters, 5(3), 154-163.

Traganos, D., & Reinartz, P. (2018). Mapping Mediterranean seagrasses with Sentinel-2 imagery. Marine pollution bulletin, 134, 197-209.

Tran, N. H., and Hall, K. D. (2007). Development and influence of statewide axle load spectra on flexible pavement performance. Transportation Research Record, 2037(1), 106-114.

Tsai, Y. C. J., Zhao, Y., Pop-Stefanov, B., & Chatterjee, A. (2021). Automatically detect and classify asphalt pavement raveling severity using 3D technology and machine learning. International Journal of Pavement Research and Technology, 14(4), 487-495.

United States Department of Transportation (USDOT, 2014). Policy and Government Affairs, Office of Highway Policy Information.

VanMeter, D., and O'Quinn, D. (2021). Safety and Operation, Weigh-in-Motion, Georgia Department of Transportation. http://www.dot.ga.gov/

Wang, K.C. (2015). Traffic and data preparation for AASHTO DARWin-ME analysis and design: [tech summary] (No. State Project No. 30000424). Louisiana Transportation Research Centre.

Wang H., Zheng H. (2013) Model Validation, Machine Learning. In: Dubitzky W., Wolkenhauer O., Cho KH., Yokota H. (eds) Encyclopedia of Systems Biology. Springer, New York, NY. https://doi.org/10.1007/978-1-4419-9863-7_233.

Wei, T. and Fricker, J. D. (2003). Weigh-in-motion data checking and imputation.

Weiss, K., Khoshgoftaar, T. M., & Wang, D. (2016). A survey of transfer learning. Journal of Big data, 3(1), 1-40.

Wiegand, K. (2018). Georgia’s Traffic Monitoring Guide. Georgia Department of Transportation. Office of Transportation Data, Atlanta, GA.

Wu, S., Wang, J., Yan, Z., Song, G., Chen, Y., Ma, Q., ... & Wu, J. (2021). Monitoring tree-crown scale autumn leaf phenology in a temperate forest with an integration of PlanetScope and drone remote sensing observations. ISPRS Journal of Photogrammetry and Remote Sensing, 171, 36-48.

Yang, H., Deng, F., Fu, H., & Zhang, J. (2021). Estimation of Rape-Cultivated Area Based on Decision Tree and Mixed Pixel Decomposition. Journal of the Indian Society of Remote Sensing, 1-8.

Zhang, A., Wang, K. C., Fei, Y., Liu, Y., Tao, S., Chen, C., ... & Li, B. (2018). Deep learning–based fully automated pavement crack detection on 3D asphalt surfaces with an improved CrackNet. Journal of Computing in Civil Engineering, 32(5), 04018041.

Zhang, Y., Song, X., Bai, B., Xing, T., Liu, C., Gao, X., ... & Xu, P. (2021). 2nd Place Solution for Waymo Open Dataset Challenge--Real-time 2D Object Detection. arXiv preprint arXiv:2106.08713.